#### **ORIGINAL PAPER**



# Investigating the rheology of fluidized and non-fluidized gas-particle beds: implications for the dynamics of geophysical flows and substrate entrainment

Eric C. P. Breard<sup>1</sup> · Luke Fullard<sup>2</sup> · Josef Dufek<sup>1</sup> · Michael Tennenbaum<sup>3,4</sup> · Alberto Fernandez Nieves<sup>3,4</sup> · Jean François Dietiker<sup>5,6</sup>

Received: 14 September 2020 / Accepted: 15 November 2021 / Published online: 7 January 2022
© The Author(s), under exclusive licence to Springer-Verlag GmbH Germany, part of Springer Nature 2021, corrected publication 2022

#### **Abstract**

Natural geophysical mass flows are among the most complex granular systems and their dynamics are often modified by the presence of an interstitial fluid. Prediction of their runout requires the development of models estimating the solid stresses in these hazardous currents wherein excess pore-fluid pressure can develop. We use discrete element modelling (DEM-CFD) with a Coarse-Graining post-processing technique (CG) to investigate the rheology of unsteady gas-particle fluidized to non-fluidized granular beds placed on horizontal and inclined planes. Similar to fluidized beds immersed in viscous fluids, the effective friction coefficient of air-fluidized beds can be defined as a function of the classic  $\mu(I)$ -rheology and the non-dimensional fluid or solid pressure to explain the failure and dynamics of granular flows with excess pore pressure on inclines. However, dilation imposed by fluid drag and particle collisions in gas-particle fluidized beds can drastically change its effective frictional properties. In contrast with the common assumption in water-particle flows that granular temperature is negligible, in our gas-particle simulations, the contribution of the velocity fluctuations to the stress tensor is significant. Hence, the shear stress is found to be non-zero even when the flow is fully fluidized in the inertial regime. These results suggest the need to better understand velocity fluctuations to predict the effective viscosity of sheared fluidized mixtures and are relevant for many applications. Notably, a unified approach is useful for many geophysical flows that encompass a range of fluidization conditions in a single flow such as pyroclastic density currents and snow avalanches.

 $\textbf{Keywords} \ \ Rheology \cdot Fluidization \cdot Pore \ pressure \cdot Geophysical \ flow \cdot Friction \cdot Dilation \cdot Pyroclastic \cdot Density \ currents \cdot Pyroclastic \cdot Py$ 

Luke Fullard and Josef Dufek: these authors have contributed equally to this work.

- Eric C. P. Breard ebreard@uoregon.edu
- Department of Earth Sciences, University of Oregon, Eugene, USA
- School of Food and Advanced Technology, Massey University, Palmerston North, New Zealand
- Department of Condensed Matter Physics, University of Barcelona, 08028 Barcelona, Spain
- ICREA-Instituci Catalana de Recerca I Estudis Avanats, 08010 Barcelona, Spain
- National Energy Technology Laboratory, U.S. Department of Energy, Morgantown, WV, USA
- Leidos Research Support Team, Pittsburgh, PA 15236-0940, USA

#### 1 Introduction

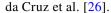
The ability of mobile granular flows to behave like liquids has fascinated scientists for centuries [25, 91] and has been the focus of studies in physics [9, 52, 62, 66, 87, 88], engineering [6, 24, 36, 75], soil mechanics [98, 110], and geology [16, 31, 53, 61]. Understanding the rheology of granular matter is essential for modelling systems with particles, but compared to single phase fluids, most constitutive approaches have been developed relatively recently. Difficulties in describing particulate systems originate from their ability to display history- and preparation-dependent strengthening and dilation [96, 111], anisotropy and normal stress differences [105], non-locality [2, 51, 68, 113], negligible thermal fluctuations, highly dissipative interactions, and a lack of separation between the microscopic grain scale and the macroscopic scale of the flow [34].



While many flows of granular media in industry can be treated as "dry" media where fluid drag can be neglected, in geophysical mass flows, particles are often fine enough to allow pore-fluid pressure to be generated and sustained for long durations [58, 60, 78, 92]. The latter case is a form of fluidization; elevated pore pressure forces a "static" solid-like granular system to behave as a liquid by having a fluid percolating through the porous media and applying a drag force opposing gravity [41, 45, 74]. With increasing superficial velocity of the fluid, the pore pressure in the bed increases up to the extent where it equals the lithostatic pressure, and the bed is thus fully fluidized. In engineering settings, fluidization is often forced by injecting a fluid near the bed and is generally used because it enhances heat transfer between the fluid and the solid [21, 82], which improves reaction rate efficiency. Additionally, mixing of a solid mixture is much easier when fluidized. Industrial fluidization is usually generated in confined systems such as cylinders or reactors. In geological settings fluidization is much more likely to occur in settings where the material is on a slope and can flow without being constrained by solid boundaries in two dimensions [93]. Typically fluidization occurs when fluid drag from escaping water or air is imposed upon the solid granular phase; This can occur, for example, as the bed compacts [13, 14, 28, 43, 57, 58, 60, 100], which occurs in debris flows and dense pyroclastic density currents. These two types of flows share many similarities. For instance, their rheology spans that of dry granular to fluidized beds and their long runout is due to the development of the pore pressure feedback [55, 77]. Yet, because the interstitial fluid in debris flows is usually made of muddy water and pyroclastic density currents of hot air, the scaling of the granular rheology differs. The rheology is dominated by the viscous number for debris flows and by the inertial number in pyroclastic density currents [77]. In addition, the mass loading of ~2 (density ratio of solid over fluid) and high viscosity of the fluid in debris flows influence the solid-fluid coupling. For instance, the lubrication force is expected to be more important in viscous liquids and affects particle interactions, the flow rheology and the solid velocity fluctuations [85].

Advances in granular physics through experiments and numerical simulations [26, 33, 34, 66] have shed light on the mechanics of granular flows. These studies show that in flows where viscous forces are negligible (Stokes number > > 1), shear stress and normal stress are correlated with a coefficient of proportionality (Eq. 1) that is the function of a single non-dimensional parameter known as the inertial number I.

$$\sigma = \mu(I)P$$
 and  $I = \frac{\dot{\gamma}d}{\sqrt{\frac{P_s}{\rho_s}}}$  (1)



Here  $\mu$  is the friction coefficient, I describes the ratio of (a) a microscopic timescale  $d/(P_s/\rho_s)^{0.5}$ , which represents the time it takes for a particle to fall in an open space of diameter d under the pressure  $P_s$ , known as the typical time scale of rearrangement, and (b) a macroscopic time scale  $1/\dot{\gamma}$  related to the average deformation. Three granular regimes have been defined based upon the scaling of the shears stress with the shear rate and the value of the inertial number. Equation (19).

When the granular flow experiences homogeneous shear, the  $\mu(I)$ -rheology (Eq. 2) approximates its mechanics and this rheology is local.

$$\mu(I) = \mu_1 + \frac{\mu_2 - \mu_1}{1 + \frac{I_0}{I}} \tag{2}$$

Jop et al 2005 [65]; Jop et al. 2006 [66] where  $\mu_1$  is the static friction coefficient, and  $I_0$  and  $\mu_2$  are material constants.

Our aim is to understand how the presence of excess pore pressure modifies the internal strength of a gas-particle granular mixture and reduces its effective viscosity. We focus on granular beds on slopes since these settings are relevant to geophysical mass flows. The novelty of our work lies in the focus on gas-particle flows with excess pore pressure in a transient state using 3D DEM-CFD simulations (i.e. partially to fully fluidized beds) whereas most of the work done on granular flows with excess pore pressure focuses on granular flows immersed in viscous fluids (e.g. water or muddy water which are dominated by viscous forces), and were investigated using experiments or two-layers depth-averaged (2D) methods [8, 34, 56].

In this paper, we use the word fluidized to describe a particulate bed with a pore pressure exceeding ambient fluid pressure (e.g. equal to atmospheric pressure in the case of flows in air) and generates fluid flow drag that opposes gravitational forces on the grains. Surprisingly, little quantitative work has been done on the rheology of sheared gas-particle fluidized beds [92, 99], although they are extremely relevant analogs for hazardous mass flows that can move rapidly downslope. Recently, continuum modelling of fully fluidized gas-particle beds using a modified Kinetic Theory (KT) has shown good agreement with experiments [64]. However, the KT suffers from limitations near the close packing limit [23], which can overpredict the runout of unsteady flows [13, 14] and has yet to be adapted to describe transient fluidized to non-fluidized granular flows. Without an understanding of the rheology of fluidized granular flows, modeling flows such as concentrated pyroclastic currents is limited and requires using simplified rheologies [48]. Even dynamics of static fluidized beds are not trivial, for instance,



experimental investigations of fluidized bed viscosity shed lights on the complexity of these system, which do not behave as pseudo-fluids [42].

The low permeability of pyroclastic flows implies pore pressure diffusion timescales that are long enough that the drag force and associated low effective viscosity operates on the mass flows for a significant fraction of their transport [13, 14]. However, since pore pressure cannot be sustained indefinitely, natural mixtures that develop pore pressure will span a whole range of behavior from fully fluidized, partially fluidized, and non-fluidized. Therefore, this study investigates the rheology of fluidized and non-fluidized beds in the framework of the  $\mu(I)$ -rheology. We explore a wide range of bulk behavior expected in the basal avalanche of natural pyroclastic density currents and other fluidized geophysical currents. We devote the study to the use of DEM-Eulerian in 3D, where the solid phase was monodisperse or slightly polydisperse and the fluid chosen to be air. The rheology is investigated numerically using a Coarse-Graining code to compute continuum fields of solid concentration, shear stress, pressure, granular temperature and shear rate.

In Sect. 3.1, we first illustrate the physical properties of a granular flow that is progressively fluidized in two contrasting settings: on a horizontal plane (i.e. confined) and on an inclined plane (i.e. unconfined), where shear can develop. Thereafter, in Sect. 3.2 we compare the scaling of the friction and solid concentration with the inertial number for fluidized and non-fluidized beds. In Sect. 4.1, we show the shear stress in fluidized beds can be defined as a function of the  $\mu$ -rheology and the effective normal stress. In Sect. 4.2, we illustrate how such definition of effective friction helps predict the behavior (acceleration, steady speed, deceleration) of a bed with excess pore pressure on a slope. In Sect. 4.3, we briefly discuss the depth-averaged approach and the relevance of our findings to the development of two-phase depth-averaged models of gas-particle flows. In Sect. 4.4, we combine the suspension and granular rheologies to describe the viscosity of fluidized beds. Finally in Sect. 4.5, we discuss the occurrence of granular flows with elevated pore pressure in natural settings and their ability to erode their substrate.

#### 2 Methods

#### 2.1 Discrete element method

In an attempt to gain insights into the relationship between rheology and the granular structure of fluidized and non-fluidized beds we model particles with the Discrete Element Method (DEM). DEM simulations are performed with the MFIX open-source code developed by the US Department Energy's National Energy Technology Laboratory (NETL). Using this method, individual particle–particle and particle–wall interactions can be simulated. Collisional and frictional contacts between particles were modeled with the soft-sphere approach using the spring-dashpot approach [38, 76]. The mixture is represented by  $N_m$  Lagrangian spheres of diameter,  $D_m$ , and solid density,  $\rho_s$ . Solving Newton's Laws of motion provides the particle momentum and position:

$$\frac{dX^{(i)}(t)}{dt} = V^{(i)}(t) \tag{3}$$

$$m^{(i)}\frac{dV^{(i)}(t)}{dt} = F_T^{(i)}(t) = m^{(i)}g + F_d^{(i \in k, m)}(t) + F_c^{(i)}(t)$$
 (4)

$$I^{(i)}\frac{d\Omega(t)}{dt} = T^{(i)}(t) \tag{5}$$

where  $X^{(i)}$  is the particle position of the i-th particle within the domain at time t,  $V^{(i)}$  is the velocity,  $\Omega$  is the angular velocity of the i-th particle,  $m^{(i)}$  is the particle mass.  $F_c^{(i)}$  is the net contact force,  $F_T^{(i)}$  is the sum of the forces acting on particle i-th,  $F_d^{(i\in k,m)}$  is the total (viscous and pressure) drag force acting on particle i, if the m-th solid phase is located within the k-th cell.  $T^{(i)}$  is the sum of the all torques acting on the i-th particle and  $I^{(i)}$  is the moment of inertia.

In the soft-sphere approach, the overlap between particles is represented by series of springs and dashpots in both tangential and normal directions. The loss of kinetic energy during inelastic collisions is modeled with the dashpot, whereas the spring models the stiffness of the solid particle—particle contact.

The coupling between the particles and the Eulerian fluid is described by the transfer of momentum between phases  $(\vec{I_f})$ , which is achieved via summing the drag force and pressure gradient force of particles located in the computational cell [[38]]:

$$\vec{I_f}(t) = \frac{1}{\nu_{REV}} \sum_{k=1}^{N_k} \vec{F_D}^{(k)}(t) K_{REV} \left( X_p^{(k)} \right)$$
 (6)

where  $K_{REV}\left(X_p^{(k)}\right)$  is a generic kernel with compact support that determines the influence of the particle force at  $X_p^{(k)}$  on the representative elementary volume  $v_{REV}$  of the  $k^{th}$  grid cell. In the first stage, the algorithm sums the weighted contribution of the particles in each cell. The second stage uses the compact support kernel to interpolate the particles properties at the fluid node as a function of the sum in the neighboring cells computed during the first stage.

The drag force  $\overrightarrow{F_D}^{(k)}$  of the particle residing in the cell k is defined as [[38]]:



$$\overrightarrow{F_D}^{(k)}(t) = -\nabla P_f(t) \left(\frac{\pi}{6} d_p^{(k)3}\right) + \frac{\beta_{fs}^{(k)}(t)}{\left(1 - \varepsilon_f(t)\right)} \left(\frac{\pi}{6} d_p^{(k)3}\right) \left(\overrightarrow{v_f}(t) - \overrightarrow{v_p}^{(k)}(t)\right)$$

$$\tag{7}$$

where  $P_f$  is the fluid pressure,  $d_p$  is the particle diameter,  $\varepsilon_f$  is the volume fraction of fluid,  $v_f$  and  $v_p$  are the fluid and particle velocity, respectively. To calculate the drag force accurately, the mean fluid-phase velocity is interpolated to the particle location. Then, the drag force on each particle is projected on the Eulerian fluid phase grid. The interphase momentum exchange term  $\rho_{fs}^{(k)}$  is evaluated via a drag model following Gidaspow (1994):

We chose to simulate particles of 0.005 m in diameter d with a density of 2500 kg.m<sup>-3</sup>. Between 4799 and 9508 particles were used with a particle–particle and particle–wall friction coefficients both set to a value of 0.5. The particle stiffness coefficients ( $k_n$  and  $k_t$ ) were chosen as  $5 \times 10^4$  Pa.m, well above the minimum required to ensure hard collisions for the pressure investigated. Based

$$\beta_{fs}^{(k)}(t) = \begin{cases}
\frac{3}{4} C_D^{(k)}(t) \frac{\rho_f \varepsilon_f(t) (1 - \varepsilon_f) \|\overrightarrow{v_f} - \overrightarrow{v_s}^{(k)}\|}{d_p^{(k)}} \varepsilon_f^{-2.56} & \varepsilon_f > 0.8 \\
\frac{150 (1 - \varepsilon_f(t))^2 \eta_f}{\varepsilon_f(t) d_p^{(k)2}} + \frac{1.75 \rho_f (1 - \varepsilon_f(t)) \|\overrightarrow{v_f} - \overrightarrow{v_s}^{(k)}(t)\|}{d_p^{(k)}} & \varepsilon_f \leq 0.8
\end{cases}$$
(8)

with  $\rho_f$  as the fluid density. The drag coefficient  $C_D^{(k)}$  is calculated as follows (*Gidaspow* 1994):

$$C_D^{(k)}(t) = \begin{cases} \frac{24}{\operatorname{Re}^{(k)}(t)(1+0.15\operatorname{Re}^{(k)}(t)^{0.687})} & \operatorname{Re}^{(k)}(t) < 1000\\ 0.44 & \operatorname{Re}^{(k)}(t) \ge 1000 \end{cases}$$
(9)

The full equations of the DEM-CFD code have been added to a supplementary tables S1 and S2. Variations of the form of the Gidaspow drag law described with a sharp or smooth transition around a voidage  $\varepsilon_f = 0.2$  does not influence our results and their interpretation (Fig. S1).

The MFIX-DEM approach has been rigorously verified in a series of studies that span monodiperse and polydisperse grain-size distributions in wall bounded flows and fluidized/spouted beds [38, 76, 84]. More information regarding the physics involved in the DEM model is provided in Garg et al. [38].

In order to assess whether lubrication forces are important, we use the scaling analysis of Carrara et al. [18], which states lubrication forces are important in a granular media solely if the following two conditions are fulfilled:

$$\log_{10}\left(\frac{Av_p}{U_T}\right) > 0 \text{ and } \log_{10}\left(\frac{Av_p}{U_T}\right) / \log_{10}\left(\frac{v_f}{2aU_T}\right) > 1 \tag{10}$$

where A expresses the relationship between the normal and tangential lubrication forces [81],  $U_T$  is the terminal fall velocity of the particles,  $v_p$  is the relative velocity between particles,  $v_f$  is the relative velocity between fluid and particles and a is the permeability parameter [5]. In our simulations,  $log_{10}\left(\frac{Av_p}{U_T}\right) < -3$  and  $log_{10}\left(\frac{Av_p}{U_T}\right)/log_{10}\left(\frac{v_f}{2aU_T}\right) < 0.4$ .

upon these physical properties, we simulate experiments to determine the angle of repose of the mixture, by imposing a periodic boundary in the spanwise direction and a domain depth equivalent to 20 particles diameter. Figure 1b shows the 3D collapse of the mixture that came to rest with a mean surface angle of 18.5°. Its tangent gives the static friction coefficient of 0.364.

As we investigate both non-fluidized and fluidized bed rheologies from DEM simulations, we perform DEM-Eulerian modeling, with the Eulerian phase chosen as air at an ambient temperature of 293.15 Kelvin and obeying the ideal gas relation (molecular weight of 28.97 g/mol). The 3D Eulerian grid spacing was chosen as 2 particle diameters in all dimensions ensuring accurate gas-particle coupling. The upper domain boundary was set as a pressure outflow with a constant set pressure of  $1.0132 \times 10^5$  Pa and the gas viscosity was calculated from the Sutherland law [102]. The mixture is gas fluidized by the use of a basal mass-inflow boundary where air at ambient temperature was injected at a controlled superficial upward velocity. In a series of 16 3D DEM-Eulerian static simulations, where both X and Z dimensions had periodic boundaries (ensuring no wall effect) we measured the gas pore pressure at the base of the column (in the lowermost cell that did not contain the static rough layer). The superficial gas velocity is plotted against the pore pressure (Fig. 1c), and shows that the minimum superficial velocity Vs of 1.85 m/s yields minimum fluidization, while bubbling occurs at a superficial velocity Vs exceeding ~ 2.0 m/s.

In order to study the rheology of fluidized and non-fluidized beds, we use a variety of DEM-CFD simulations that are summarized below. The investigation required



Fig. 1 a DEM-CFD setup composed of a bed (white), that is constrained between the sheared top rough layer (red) and a bottom static rough layer (blue). b: DEM-CFD simulation of a dam-break collapse of the granular mixture of 5 mm beads in 3D. Periodic boundaries were used in the Z direction (normal to the plane shown), and the depth of the domain was equal to 0.05 m. DEM-CFD parameters used are summarized in Table 1. c: Results of 16 steady state simulations are shown, by plotting the superficial gas (air) velocity versus the pore fluid pressure at the base of a 0.1 m thick bed of 5 mm beads (Table 1, for physical properties)

a set of simulations where we changed individually the boundary parameters: confined or unconfined, gas-fluidized or non-fluidized and the initial conditions of the setup: on a slope, with or without a confining pressure and with or without a rough erodible bed.

Each set of numerical experiments focused on a distinct portion of the fluidized/non-fluidized parameter space and is presented in the order of their appearance in figures.

#### 2.1.1 Fluidized bed

#### Type 1.1: Confined.

In this simulation we modelled the progressive fluidization (increase at rate of 0.2 m/s<sup>-2</sup>) of a bed confined by periodic boundaries and on a horizontal plane. A rough base of 361 particles of 0.005 m diameter was implemented in the model and made static at all times. 8747 particles were initially distributed in a 3D lattice with an initial, isotropic, granular temperature ensuring 'random' collisions during collapse.

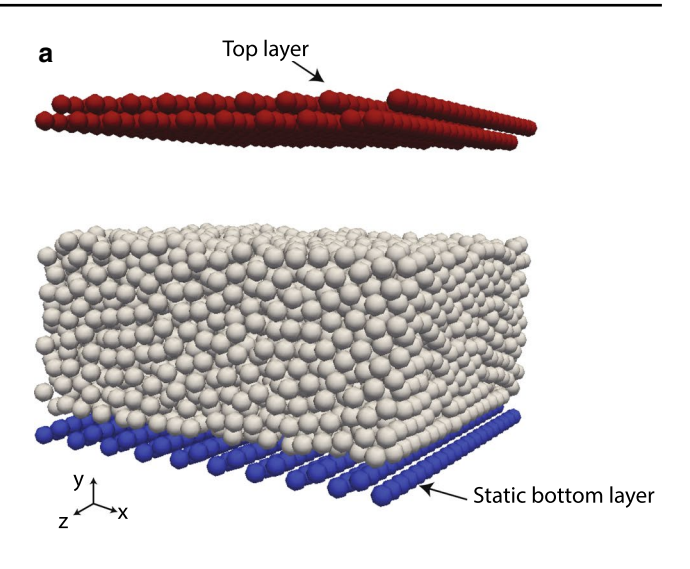
*Type 1.2 : Destabilization by fluidization on a slope.* 

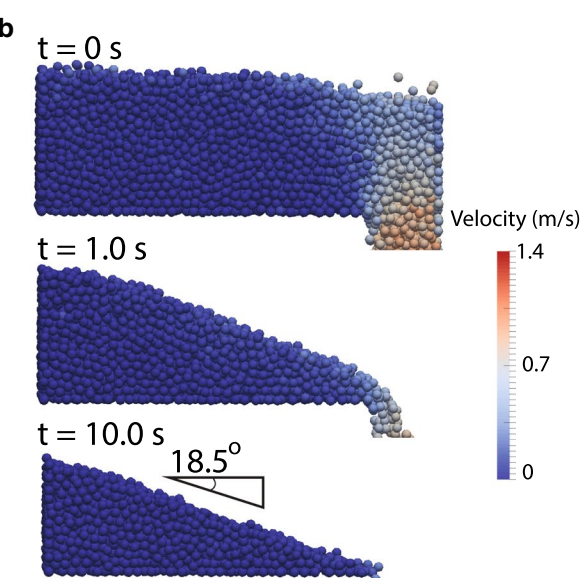
We used this technique to recover the  $\mu(I)$ -rheology and  $\Phi(I)$  of fluidized beds by setting the slope constant and changing the superficial velocity over time (0.04 m/s per sec). This type of simulation was used to understand the scaling between the dimensionless pore pressure and the dimensionless solid pressure. Sensitivity testes indicate the results are independent of the value of superficial gas acceleration chosen (Fig. S2).

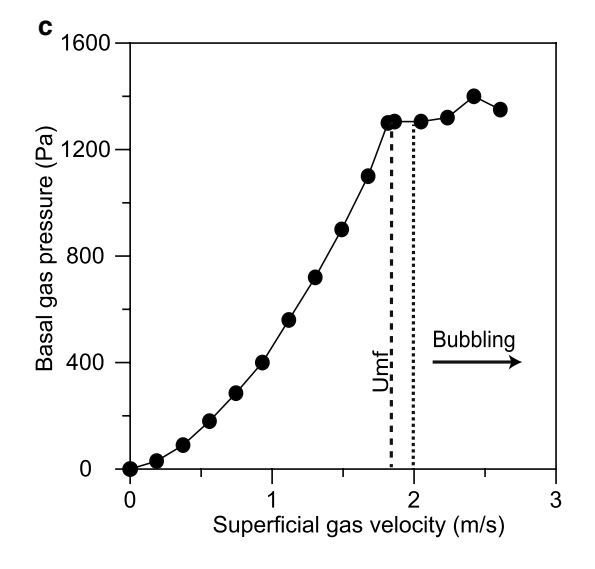
#### 2.1.2 Non-fluidized bed

*Type 2.1 : Destabilization of beds with free-surface.* 

This setup technique was used to recover the  $\mu(I)$ -rheology and  $\Phi(I)$  of non-fluidized granular beds. We modelled the slow destabilization of a bed of 4419 particles by rotating gravity over time (simulating increasing inclination









**34** Page 6 of 25 E. C. P. Breard et al.

of the bed), at a slow rate of  $\frac{0.2\pi}{180}$  rad.s<sup>-1</sup>, which is half an order of magnitude lower than the relaxation rate of the bed found to be ~ 1.1 rad.s<sup>-1</sup> to ensure these are pseudo-steady conditions. The lower boundary was made of particles, forced to be static, and every second row was displaced upward by 0.5 particle diameter, to ensure a no-slip boundary condition. We separately varied the contact stiffness and restitution coefficient in order to assess their effect on the flow rheology across the quasistatic, intermediate and inertial regimes.

We also compare the monodisperse mixture of 5 mm spherical particles with a slightly polydisperse size distribution with three size fractions in the following proportions of their diameter: 1/3 of 4, 1/3 of 5 and 1/3 of 6 mm.

#### Type 2.2: Shear cell.

In these 200 simulations, we aimed at recovering the  $\mu(I)$ -rheology and  $\Phi(I)$  for a wide range of inertial numbers  $(10^{-6}-2\times10^0)$  in a steady state, which allowed us to compare our results with the destabilization simulations (type 2.1). In the setup, the bottom plate was static while the top plate velocity was imposed to shear the bed. The plate could move up and down to keep a constant confining pressure.

#### 2.1.3 Erodible substrate

*Type 3: Shear cell with erodible bed.* 

These simulations compared the mobilization of an erodible substrate by a granular flow with and without the effect of excess pore pressure. A bed of 4799 particles was sheared by setting the rough top plate of 361 particles with a velocity of 5 m/s, and an erodible bed made of 8747 particles was sitting atop a rough static plate of 361 particles. The

fluidized case was achieved by having a superficial velocity of 2.0 m/s.

To illustrate in more details the role of granular temperature on the non-local behavior of granular flows propagating upon an erodible substrate, we ran 23 shear cell simulations with 35,984 particles. The bed was confined between a bottom rough static plate and a top rough plate to which we attributed a velocity from 0.0001 to 100 m/s and a constant pressure of 8 kPa. All particles with a position < 0.14 m were set with a 0 velocity until the bed of  $\sim$  0.05 m of thickness reached steady state. After 15 s, the rough substrate was able to respond to the shear flow above. There was no excess pore fluid pressure in any of the 23 simulations.

Unless stipulated otherwise, the DEM-CFD simulation parameters used are summarized in Table 1. For clarity, we indicated in Table 2 the type of simulation used to generate the data provided by all figures involving the DEM-CFD.

#### a. Coarse graining

The coarse graining method (CG) is a computational tool designed to study discrete systems (e.g. DEM-CFD simulations) and built to calculate continuum fields, in

**Table 2** Types of DEM-CFD simulation from which the data is exported and presented in the different figures of the manuscript

Figure #	DEM-CFD simulation type	
2	1.1	
3	1.2	
4	2.1 and 2.2	
5	1.2 and 2.1	
6	1.2	
7	1.2	
8	1.2	
9	1.2 and 2.1	
10	3	
11	3	

**Table 1** Summary of the DEM-CFD simulation parameters used by default. Additionally, a set of simulations involved changing a single parameter, thus keeping all other quantities equal

Parameter [units]	Variables	Values	
Domain size [m]	x, y, z	$0.1 \times 0.5 \times 0.1$	
Grid size [m]	DX, DY, DZ	0.01	
Fluid temperature [K]	$T_{g}$	293.15	
Fluid dynamic viscosity [Pa s]	0	$\mu_f$	$1.8 \times 10^{-5}$
Particle density [kg.m <sup>-3</sup> ]		$ ho_f$	2500
Particle diameter [m]		$d_p$	0.005
Initial bed height [m]		$\dot{H_0}$	0.1
Number of particles	N	9508	
Particle stiffness (normal) [N.m <sup>-1</sup> ]	$k_n$	$5 \times 10^4$	
Particle normal restitution coefficient	$e_n$	0.5	
Particle coefficient of friction	$\mu_{p-p}$	0.5	
Particle–wall coefficient of friction	$\mu_{p ext{-}w}$	0.5	



particular the stress tensor. The CG method has advantages over other methods in its ability to create fields that satisfy the conservation equations of continuum mechanics even for small numbers of particles, and does not require an assumption of particle shape or stiffness. The sole assumptions are that each contact between two particles is a "point contact" and collisions are not instantaneous. Multiple studies have successfully involved CG for granular flows in numerical [104, 106, 107], experimental studies [63, 97] and even molecular flows [50].

Note that the "coarse-graining" term may be ambiguous since it consists in molecular dynamics in replacing an atomistic description with a collection of molecules, and similarly this is applied for DEM of granular flows to describe a continuum of a collection of multiple particles [89]. In this paper, it is applied to the micro-macro transition method developed in Babic [3] and extended by Weinhart et al. [106].

The mixture total stress tensor is simply the sum of the kinetic and contact stress tensors:

$$\sigma(r,t) = \sigma^k(r,t) + \sigma^c(r,t) \tag{11}$$

where the kinetic tensor depends on particle velocity fluctuations and the contact tensor depends on the contact forces. The full description of the tensors is provided in the Supplementary Information.

The granular friction coefficient is calculated from the 2D version of the stress tensor in combination with the pressure using all 3 contributions, which is the best approach for plane shear configuration [23, 37, 85, 106, 113].

$$\mu = \frac{\left|\sigma^{D}\right|}{P_{c}}\tag{12}$$

where

$$\left|\sigma^{D}\right| = \sqrt{0.5 \ \sigma_{ij}^{\prime D} \sigma_{ij}^{\prime D}} \tag{13}$$

All the data presented in this manuscript are for beds that are yielding (i.e. where a shear rate is measurable).

The average normal stress or solid pressure in the system is calculated as the trace of the 3D stress tensor:

$$P_s = \frac{1}{3}tr(\sigma) \tag{14}$$

The granular temperature inside the mixture is defined as:

$$T_g = \frac{tr(\sigma^k)}{3\rho} \tag{15}$$

One essential parameter to scale the friction coefficient and solid concentration is the inertial number:

$$I = \frac{\dot{\gamma} d}{\sqrt{\frac{\dot{P}_s}{\rho_s}}} \tag{16}$$

where  $\rho_s$  is the solid density,  $\dot{\gamma}$  is the shear rate, d is the mean particle diameter.

For polydisperse systems, the inertial number is calculated with the volumetrically averaged particle diameter *d* known as the D43 [46]:

$$d' = D_{43} = n_q d_q$$
 (17)

Throughout the text, we use the term pore pressure to refer to the differential pore fluid pressure (absolute pore fluid pressure—ambient absolute pressure of the fluid phase).

In this manuscript, the term lithostatic pressure refers to the bed weight per unit area when non-fluidized, which is the depth-integrated normal stress. For instance, a bed with an excess pore pressure of 50%, consists in a bed where the pore pressure/lithostatic pressure = 0.5. When the pore pressure = lithostatic pressure, the bed is fully fluidized.

#### 3 Results

## 3.1 Numerical rheology

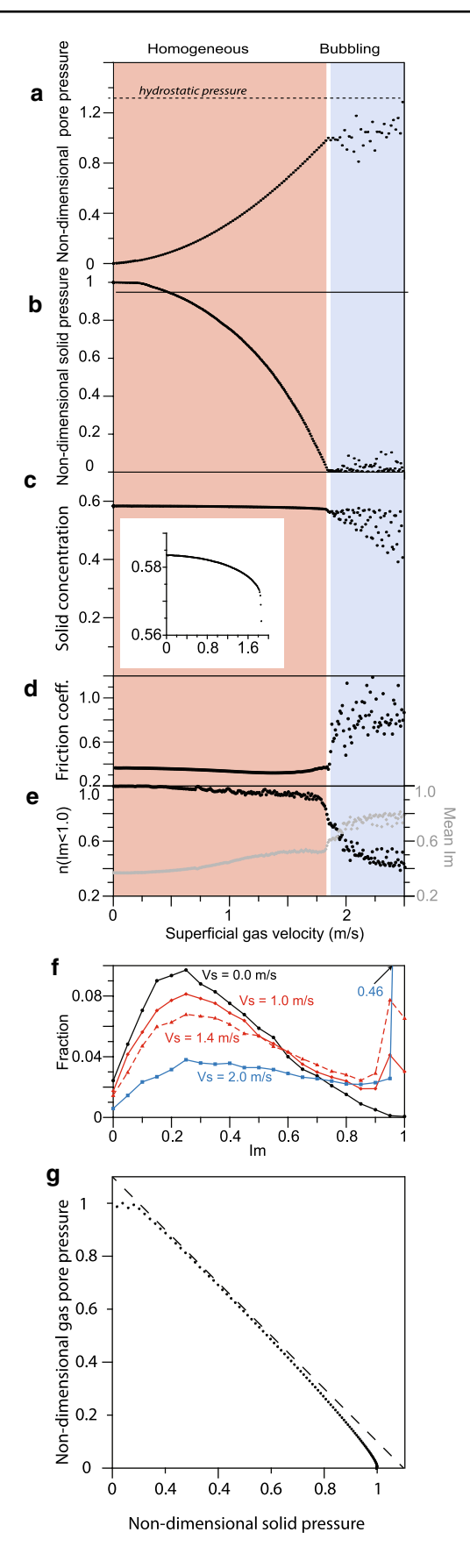
#### 3.1.1 Confined fluidized bed

A detailed and predictive description of the viscosity of granular beds has remained elusive [42, 44]. Measurements are extremely difficult to achieve in practice and if undertaken with a two-stirrer rheometer blade, physical properties such as the solid pressure remain unknown and the shear rate is heterogeneous. Here, we use a CG analysis to calculate the effective viscosity of fluidized beds with air. In the following sections, the rheology of a bed confined and on a horizontal plane is illustrated as it progressively transforms from a nonfluidized media into a fully fluidized and bubbling bed. We then compare the evolution of the same bed undergoing similar transitions (non-fluidized to bubbling) when unconfined (i.e. can flow) and placed on an inclined plane. Next, we confirm that steady and unsteady (i.e. transient) beds display the same rheology. Finally, the similarities between fluidized and non-fluidized granular flow rheologies are demonstrated. Finally, most granular flows simulated are in a transient state where the slope or excess pore pressure changes over time, which is relevant to natural and experimental geophysical applications.



Fig. 2 Fluidization simulation of a confined bed on a horizontal > plane. The CG analysis was undertaken in the lower 0.04 m above the rough substrate. The solid pressure (a), solid concentration (c), friction coefficient (d), proportion of particle contacts n (Im < 1.0) that not sliding and average Friction Mobilization Factor (e) are plotted, while the excess pore pressure (b) data shown is at 0.005 m above the rough plate. The insert in (c) shows the concentration (y-axis) as a function of the superficial gas velocity (x-axis) and illustrate the small but measurable dilation that occurs. For all particle contacts, we calculated the Friction Mobilization Index (Im), which is the ratio Ft/ (Fn  $\times \mu_{pp}$ ), where Ft and Fn are the magnitude of the tangential and normal contact force, respectively, and  $\mu_{pp}$  is the particle-particle friction coefficient we used in the DEM code (=0.5). The distribution of Im for all contacts are shown at four different superficial velocities (V<sub>s</sub>) in (f). A contact is mobilized (i.e. sliding occurs between two particles) when Im=1. Non-dimensional excess pore pressure is plotted against the non-dimensional solid pressure for the homogenous regime (g). The pore pressure and solid pressure are scaled to the lithostatic pressure measured when no air is injected in the mixture (non-fluidized). The red background highlights the homogeneous regime, devoid of bubbles and prior to minimum fluidization at  $V_s = V_{mf} \sim 1.85$  m/s. The blue background shows the bubbling regime, where bubbles propagate upward through the bed

To illustrate the evolution of the rheology of non-fluidized to fully fluidized beds, we run a DEM-CFD simulation where the superficial gas velocity starts at 0 m/s and slowly increased at a rate of 0.2 m/s<sup>-2</sup>. Data is exported from these simulations every 50 ms for CG analysis. We illustrate the evolution of the bed rheology at various porefluid pressures using the CG for the lowermost half of the bed (0-0.04 m above the bottom rough plate). From superficial gas velocity of 0-1.85 m/s, the flow is homogeneously fluidized and no bubbles form. The data shows no fluctuations despite the lack of time-averaging. In the homogeneous stage, the pore pressure increases (Fig. 2a) and the solid pressure decreases (Fig. 2b) non-linearly as the superficial gas velocity increases. Meanwhile, the solid concentration shows little variation (~1 vol.%) from non-fluidized to the onset of minimum fluidization at  $V_s = V_{mf} \sim 1.8-1.85$  m/s (Fig. 2d). At the minimum fluidization, the fractional solid and gas pressure reach 0.1% and 99.9% of the lithostatic pressure. Subsequently, the friction coefficient decreases from the static value of 0.355 to 0.3. The weak dilation the bed experiences (See insert of Fig. 2c) is also followed by a reduction of the number of contacts by 4% between  $V_s = 0$  m/s to  $V_s = 1.4$  m/s when the friction coefficient is lowest. We illustrated the Frictio-Mobilization Index (Im), which is the ratio Ft/(Fn  $\times \mu_{nn}$ ), where Ft and Fn are the magnitude of the tangential and normal contact force, respectively.  $\mu_{pp}$  is the particle–particle friction coefficient we used in the DEM code (=0.5). Such a parameter can be useful to understand liquefaction [49, 112]. At each timestep, a distribution of *Im* for all particle contacts provides a mean of the distribution and number of contacts with Im < 1, which indicates the yield state





of the system since all contacts with Im < 1 are not sliding (or fully mobilized) (Fig. 2e). The distribution between  $V_s = 0$  m/s,  $V_s = 1$  m/s and  $V_s = 1.4$  m/s are relatively similar for Im < 0.9 (decline of proportion of contacts with increase of Im) but the increase in the proportion of contacts with Im = 1 and near sliding (Im > 0.9) illustrates the yield of the system despite measuring a friction coefficient below the static friction coefficient of ~0.36. While the bed is dilating and prior to being fully fluidized, there is only partial mobilization of the friction between particles.

When the superficial velocity equals ~ 1.9 m/s, bubbles form and are accompanied by the large fluctuations in gas and solid pressures, concentration and friction coefficient. Note that the friction coefficient increases drastically from V<sub>mf</sub> onwards as particle collisions increase. This is also illustrated in the distribution of the Friction Mobilization Index, where ~46% of contacts are sliding. Typically, it is assumed in static fluidization experiments that the pore pressure is a proxy to the solid pressure in the homogeneous phase (Roche et al. 2012). This calculation shows that the pore pressure scales linearly (slope of 1) with the solid pressure except at the low superficial velocities (0–10% of  $V_{mf}$ ).

In summary, the decline of the friction coefficient (below static friction) prior to bubbling is attributed to the partial mobilization of the friction (sliding) which is induced by the slight dilation of the bed due to the presence of excess pore pressure. The waning of the friction coefficient below the static friction coefficient is expected only in settings where the bed cannot "flow" to respond to the change of effective stresses because it is confined. Once enough contacts are mobilized (~20%, see Fig. 2e), the friction coefficient of the bed exceeds the static friction coefficient.

Most engineering studies focus on static fluidized beds. However, in geological settings, pore-fluid pressure can develop in debris flows or pyroclastic flows that propagate on inclined surfaces and in configurations where the bed is not confined in 2D. Thus, in the next section, we examine the rheology of the fluidized bed on an incline.

#### 3.1.2 Fluidized bed on a slope

Using DEM-CFD, we show how pore pressure evolution modifies the granular bed rheology from dry to fully fluidized, as this whole range of behavior is expected to occur in geophysical flows. Flowing of the mixture is achieved by inclining gravity to mimic a 24° slope. At such an angle, the bed rapidly reaches steady state devoid of pore pressure (<10 s) and gas is injected in the lower boundary afterwards. The CG analysis results and pressure data are exported at every 50 ms. Note that the minimum fluidization is reached at superficial velocity of 4.46 m/s. Above this gas velocity, the bed starts bubbling. Noticeably, the onset of bubbling coincides with a sudden change in slopes for all parameters plotted against superficial velocity. The behavior of the fluidized bed is very different from that of the confined bed. While the gas pore-pressure increases and the solid pressure decreases with increasing superficial velocity, the pore pressure reaches the solid lithostatic pressure at V<sub>mf</sub> (i.e. balances the lithostatic pressure) whereas the average solid pressure remains fluctuating around 18% of lithostatic pressure (Fig. 3a and b). Subsequently, the solid concentration rapidly drops from 58% to reach 20% at V<sub>mf</sub> (Fig. 3c). Meanwhile, the friction coefficient increases systematically (well above the static friction coefficient) with superficial velocity and reaches a plateau around a value of 1.1 in the bubbling regime (Fig. 3d).

Fluctuations are higher for all properties than in the confined case (see Fig. 2). The non-dimensional pore pressure against the non-dimensional solid pressure falls along the slope of one, up to a non-dimensional solid pressure of 0.4 (Fig. 3e). Note that the solid pressure never goes to zero, because particle collisions and velocity fluctuations never vanish.

## 3.2 $\mu(I)$ -rheology and $\Phi(I)$ of pressure balanced and fluidized beds

## 3.2.1 Instantaneous versus time-averaged rheology of pressure-balanced beds

We investigate the role of pore pressure on the granular bed and how the bed responds to the change of normal stress (alleviated by the formation of pore pressure). We first present results from simulations where the bed is immersed in air with a pore pressure equilibrated to the ambient (without excess pore pressure or pressure balanced) and the bed is confined only by its own weight. A similar approach was used in other granular rheology studies but typically there was no interstitial fluid phase [67, 105]. Here we compare the rheology determined from "instantaneous" CG analysis that involved the averaging of two timesteps (100 ms apart) on an unconfined bed (no top plate) versus time-averaging of 1000 time steps from shear cell simulations (data recorded during 100 s). In the instantaneous case, we rotate the gravity vector slowly, whereas the time-averaged data involved 100 individual simulations of a sheared bed confined by two rough plates, wherein a force and velocity are imposed on the upper rough plate (Fig. 1a). The wide range of inertial number spanning  $1 \times 10^{-6}$  to  $2 \times 10^{0}$  is investigated by changing either pressure or the shear rate in the shear cell simulations. In Fig. 4a, we plot the  $\Phi$  as a function of the log of the inertial number  $\log_{10}(I)$ . Because there are very few fluctuations in the data, the  $\Phi(I)$  law is directly recovered and takes the form:



**34** Page 10 of 25 E. C. P. Breard et al.

Fig. 3 Fluidization simulation of a sheared bed on a  $24^\circ$  slope. The solid pressure (a), solid concentration (c) and friction coefficient (d) are plotted, while the pore pressure (b) data shown is at 0.005 m above the rough plate. Non-dimensional pore pressure is plotted against the non-dimensional solid pressure for the homogenous fluidization regime. The dashed line shows a slope of 1. The pore pressure and solid pressure are scaled to the lithostatic pressure at the measurement location when no air is injected in the mixture (non-fluidized). The red background highlights the homogeneous regime, devoid of bubbles and prior to minimum fluidization at  $V_s = V_{mf} = 4.46$  m/s. Bubbling is highlighted with the blue background whereas homogenous fluidization is shown with the red background

$$\Phi(I) = \frac{\Phi_{\text{max}}}{1 + aI} \tag{18}$$

with  $\Phi_{\rm max}$  being the maximum concentration and a being a constant found by fitting. The fit gives  $\Phi_{\rm max} = 0.583$  and  $a \sim 1.0$ .

Plotting the time-averaged CG data reveals that the time-averaged data fall within the field of instantaneous data (Fig. 4b) and for inertial numbers below  $10^{-5}$ , the friction coefficient is fairly constant. We fitted the classical  $\mu(I)$ -rheology (Eq. 2) [66] to the instantaneous data, with  $\mu_1$ =0.355, which is the static friction coefficient,  $\mu_2$  = 1.04 and  $I_0$  = 0.289 (Fig. 4c). The good fit to the data however is restricted to I < 0.6, as illustrated for the complete dataset of time-averaged data (Fig. 4d). In fact, the  $\mu(I)$ -rheology predicts a plateau for the friction coefficient, whereas the data diverge from that law. The best fit to the time-averaged data using the Eq. (2) gives  $\mu_1$ =0.355, which is the static friction coefficient,  $\mu_2$  = 1.43 and  $I_0$  = 0.81 (Fig. 7e). While it better matches the data for I>0.6, the fit in the intermediate regime at I>10<sup>-3</sup> to 0.3 is fairly poor.

In order to describe the rapid increase of the friction coefficient with I at large inertial numbers, we plotted the following  $\mu(I)$  law based upon the work of Holyoake and McElwaine [52]:

$$\mu(I) = \frac{\mu_s I_0 + \mu_d I + \mu_\infty I^2}{I_0 + I} \tag{19}$$

which involves the same parameters as in the classical  $\mu(I)$ , with  $\mu_s$  is the static friction coefficient =  $\mu_1$ ,  $\mu_d = \mu_2$  and  $I_0$ . There are also other constants that can be found by fitting the data such as  $\mu_{\infty}$ . By fitting Eq. (19) to the data we found  $\mu_1 = 0.355$ ,  $\mu_2 = 1.0$ ,  $I_0 = 0.3$  and  $\mu_{\infty} = 0.18$  (Fig. 7f). This provides a good agreement with the data for the whole range of inertial number investigated and suggests that a single simulation can be used to recover the  $\mu(I)$  instead of using laboriously tens of individual simulations. This is very handy, in particular to investigate the role of DEM-CFD parameters or even to look at the effect of pore pressure

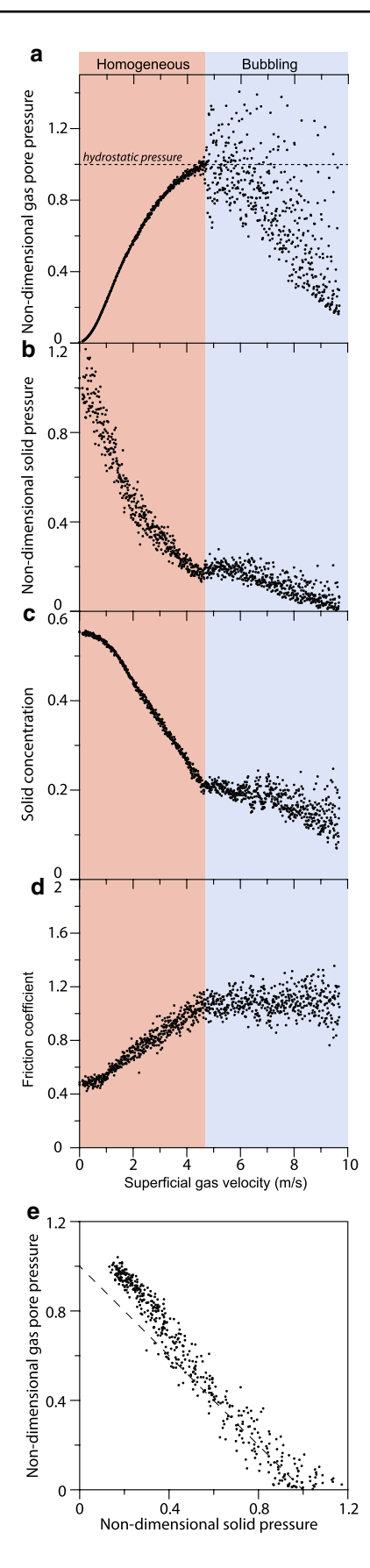
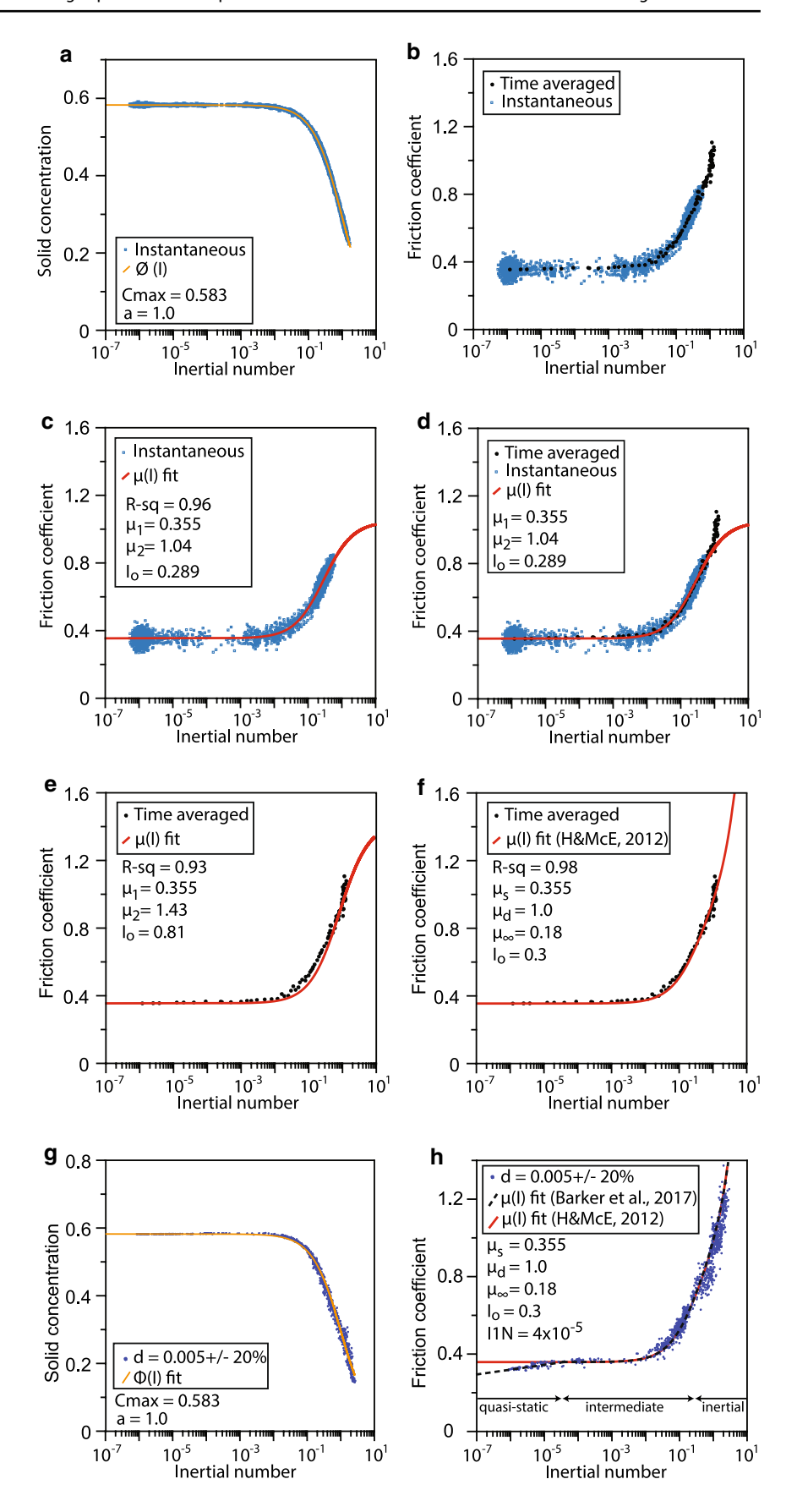




Fig. 4 Rheology of the non-fluidized bed. a: Solid concentration versus inertial number for the instantaneous CG analysis. b: Time-averaged (each black data point is an individual simulation) versus instantaneous friction data (blue dots) against inertial number calculated from the CG analysis. c: Instantaneous friction data with the  $\mu(I)$  fit (red line) was added [66] with the fitting parameters shown in the legend. d: Instantaneous and time-averaged friction data with the  $\mu(I)$  fit from figure (c). e:  $\mu(I)$  fit [66] to the time-averaged data. **f**:  $\mu(I)$  fit from Holyoake and McElwaine [52] to the time-averaged data. g: Solid fraction versus inertial number for the slightly polydisperse bed of particle diameter  $5 \pm 1$  mm. The yellow line represents to fits to the data in figure a. h: Friction versus inertial number for the same mixture as in (g). The red line is the fit from (f), and the black dotted line is the description of Barker et al. [4] (Eqs. 20 and 21)





on the granular rheology. Interested readers can visualize how the particle softness and particle restitution coefficient affect the bulk  $\mu(I)$  and  $\Phi(I)$  scaling (Fig. S4), which are commensurate with earlier findings of Chialvo et al. [22]. In addition, the presence of the interstitial fluid (air), which was included for completeness, has no measurable influence on the results and could have been excluded from simulations where no-excess pore pressure was investigated.

In order to check whether slight polydispersity could affect the flow rheology, we reproduce the polydispersity of  $d \pm 0.2d$  used in the rheology experiments. The mean particle diameter was calculated at each timestep to account for size segregation in the CG analysis. The solid density follows the same trends as the monodisperse case (Fig. 4g). Additionally, the friction coefficient also follows the same trend as the monodisperse counterparts for the intermediate and inertial regimes. However, there is evidence of the thermal creep regime in the data for  $I < 4 \times 10^{-5}$ , as suggested by the friction coefficient that becomes lower than the tangent of the angle of repose (=0.355). The fit thus requires the addition of the description of the decline of the friction coefficient with I for low inertial number, which has conveniently been provided by Barker et al. [4]. By adding a function describing the lowering of the friction coefficient below the static friction coefficient, one can describe the quasistatic, intermediate and inertial regimes with the following function:

$$\mu(I) = \begin{pmatrix} \sqrt{\frac{\alpha}{\ln\left(\frac{A_1}{I}\right)}} & I \le I_1^N \\ Eq.21 & I > I_1^N \end{pmatrix}$$
 (20)

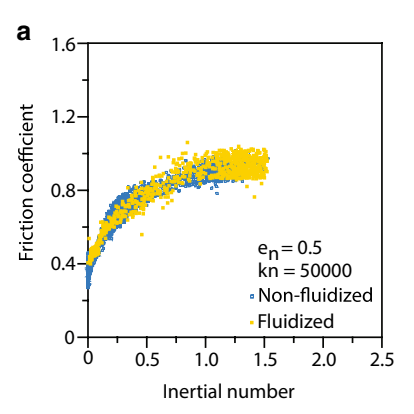
$$A_{1} = I_{1}^{N} \exp\left(\frac{\alpha \left(I_{0} + I_{1}^{N}\right)^{2}}{\left(\mu_{static}I_{0} + \mu_{d}I_{1}^{N} + \mu_{\infty}(I_{1}^{N})^{2}\right)^{2}}\right)$$
(21)

where  $A_1$ ,  $I_0$ ,  $I_1^N$ ,  $\mu_\infty$ ,  $\mu_d$  and  $\alpha$  are constants. When used in continuum models, Eqs. (20) and (21) ensure well-posedness for I = 0 to  $\sim 10$  (Barker et al. [4]).

Because the friction coefficient only differs from monodisperse at very low inertial numbers  $< \sim 10^{-5}$  and because the role of polydispersity is beyond the scope of the present work, the following sections solely focus on monodisperse suspensions.

#### 3.2.2 Non-fluidized versus fluidized bed rheology

In this section we qualitatively compare the rheology of sheared fluidized beds with that of the non-fluidized sheared beds. A good overlap for the  $\mu(I)$  exists between the sheared fluidized and the non-fluidized beds for the intermediate and inertial regime. This is shown by adding the  $\mu(I)$  fit from the time-averaged rheology simulations (from Fig. 5a, b),



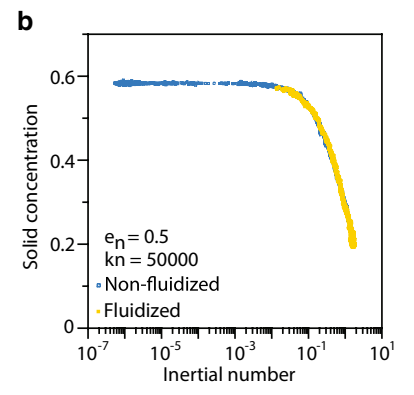


Fig. 5 Scaling of the friction coefficient (a) and solid concentration (b) against the inertial number for the sheared non-fluidized and fluidized beds

which shows that it describes well the increase of  $\mu$  at high inertial numbers.

### 4 Discussion

# 4.1 Friction coefficient in beds with excess pore pressure

Granular flow rheology is independent of the absolute pore pressure of the fluid phase in which it is immersed. However, pore fluid flow driven by pore pressure gradients and specifically excess pore pressure can modify the effective stresses in granular flows. This is particularly common in beds with a vertical gas flux, where the drag force opposes gravity and is known as fluidization. Fluidization (excess pore pressure) lowers the initial measured friction coefficient  $\mu(I)$  in fluidized beds confined in a volume (bed dilates but does not flow in directions normal to gravity). This behavior is the result of drag-induced dilation, where friction is partially mobilized.

By contrast, in granular beds with excess pore pressure, which are allowed to flow (i.e. placed on an incline, or not



physically constrained) depict a  $\mu(I)$  systematically greater than the static friction coefficient due to particle collisions.

However, dam-break experiments on initially to partially fluidized beds show that the angle of repose is much lower than the angle of repose of the material in a non-fluidized state [94]. Obtaining information regarding the friction properties of fluidized beds from such experiments is not possible since the flows are highly unsteady. Below, we reconcile our experimental observations of similar  $\mu(I)$  between the fluidized and non-fluidized bed, the low angle of repose of fluidized bed from damn-break experiments and the  $\mu(I)$ -rheology measured in DEM-CFD simulations.

Most interesting is the effective friction of the bed and whether it equals the macroscopic friction, in particular for a sheared fluidized bed. We showed that the  $\mu(I)$ -rheology of non-fluidized bed is similar to that of the fluidized counterpart. Such behavior entails that when fluidized, the solid pressure is significantly lower than lithostatic, thus raising the inertial number. Therefore, a question arising is whether sheared fluidized beds can reach steady state? On a 24° slope, we simulate a fluidized bed with a chosen superficial velocity of 1.5 m/s. For 7 s the flow was in a transient state before the solid concentration (Fig. 6a), solid pressure (Fig. 6b), shear rate (Fig. 6c), inertial number (Fig. 6d) and friction coefficient (Fig. 6e) become constant. Once steady, we notice that the macroscopic friction coefficient of  $\sim 0.55$ largely exceeds the tan(slope) = 0.445 (Fig. 6e), which by itself should prevent steady state to occur and suggest that the flow should progressively slow down.

We define the non-dimensional solid  $P_s^*$  (Fig. 6a) and pore pressure  $P_a^*$  (Fig. 6b) where:

$$P_g^* = \frac{P_g}{P_{lithostatic}} = \frac{P_g}{\rho g h}$$
 and  $P_s^* = \frac{P_s}{P_{lithostatic}} = \frac{P_s}{\rho g h}$  (22)

The effective friction coefficients as either the ratio of the macroscopic friction and non-dimensional solid pressure or non-dimensional pore fluid pressure (Fig. 6h).

$$\mu_{eff}(I, P_g^*) = \mu(I)(1 - \alpha P_g^*)$$
 and  $\mu_{eff}(I, P_s^*) = \mu(I)P_s^*$ 
(23)

 $\alpha$  is a coefficient that needs to be fitted and corresponds to the slope of the linear approximation of Ps\* = f(Pg\*), and takes a value of ~0.85 ± 0.05 in calculations of the effective friction coefficient (Fig. 6f and g). The effective friction coefficients tend to tan(slope), thus explaining how steady state can be attained. This means that the effective friction coefficient needs to account for the degree of bed support either through the reduction of solid pressure or increase of pore fluid pressure to describe accurately a granular flow with pore pressure.

While the partially fluidized bed follows the  $\mu(I)$ -rheology (Fig. 5), it behaves as a bed of equal mass on a steeper

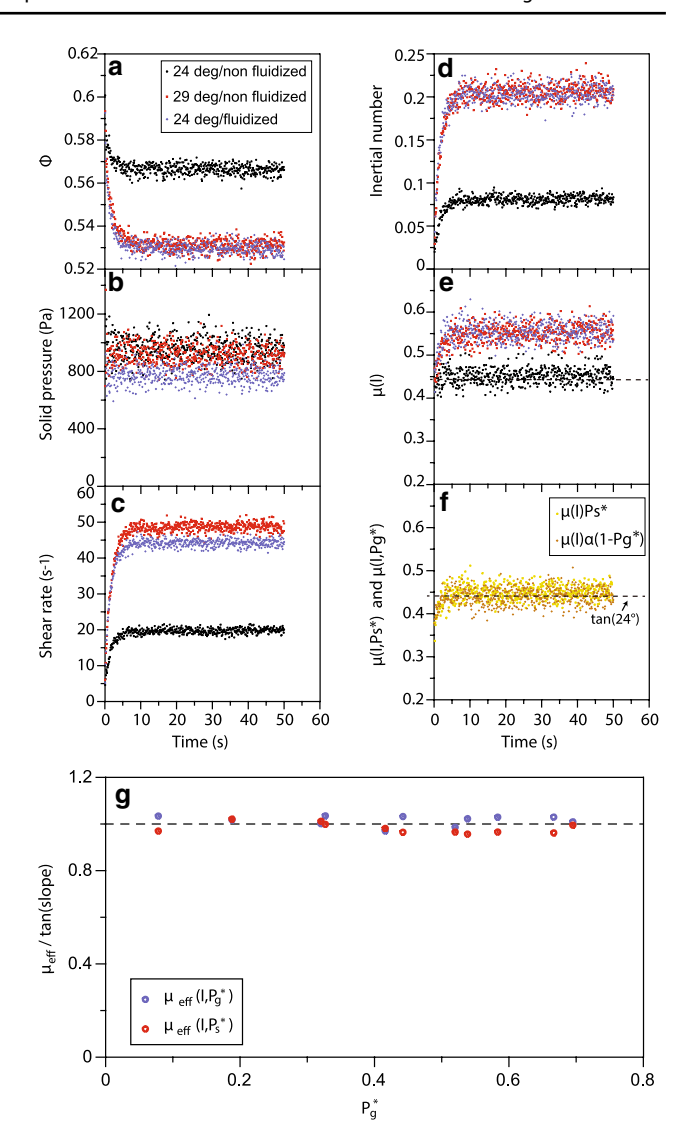


**Fig. 6** Effective friction coefficient of granular beds with pore pressure. Shear rate (a), solid concentration (b), non-dimensional pore pressure  $P_g^*$  (c) and friction data  $\mu(I)$  (d) versus time for a sheared partially fluidized bed on a 24° slope. The gray background illustrates the transient state. In (f), the dashed line represents the  $\tan(\text{slope}) = 0.445$ . In figures e and f, the friction coefficient  $\mu$  is corrected and named effective friction coefficient  $\mu_{\text{eff}}$ . In f,  $\mu_{\text{eff}} (I, P_g^*) = \mu(I) \left(1 - \alpha P_g^*\right)$  and  $\mu_{\text{eff}} (I, P_s^*) = \mu(I) P_s^*$ . g: Plot of  $\mu_{\text{eff}} (I, P_g^*) = \mu(I) P_s^*$ . Pg\*=0 when the bed has no excess pore pressure

slope. Figure 6 shows that the dry bed on a 29° slope display the same i) inertial number, ii)  $\mu(I)$ , iii) solid concentration, but because the solid pressure of the fluidized bed is slightly lower, the shear rate is also lower than in the 29°-dry case. The value of 29° is found by simply taking the arc tangent of time-averaged  $\mu(I)$  of the 24° fluidized case.

Following this finding, we investigate the steady state of fluidized beds under a range of pressures and slopes covering 15–30°. When the bed reaches steady states, the effective



**34** Page 14 of 25 E. C. P. Breard et al.

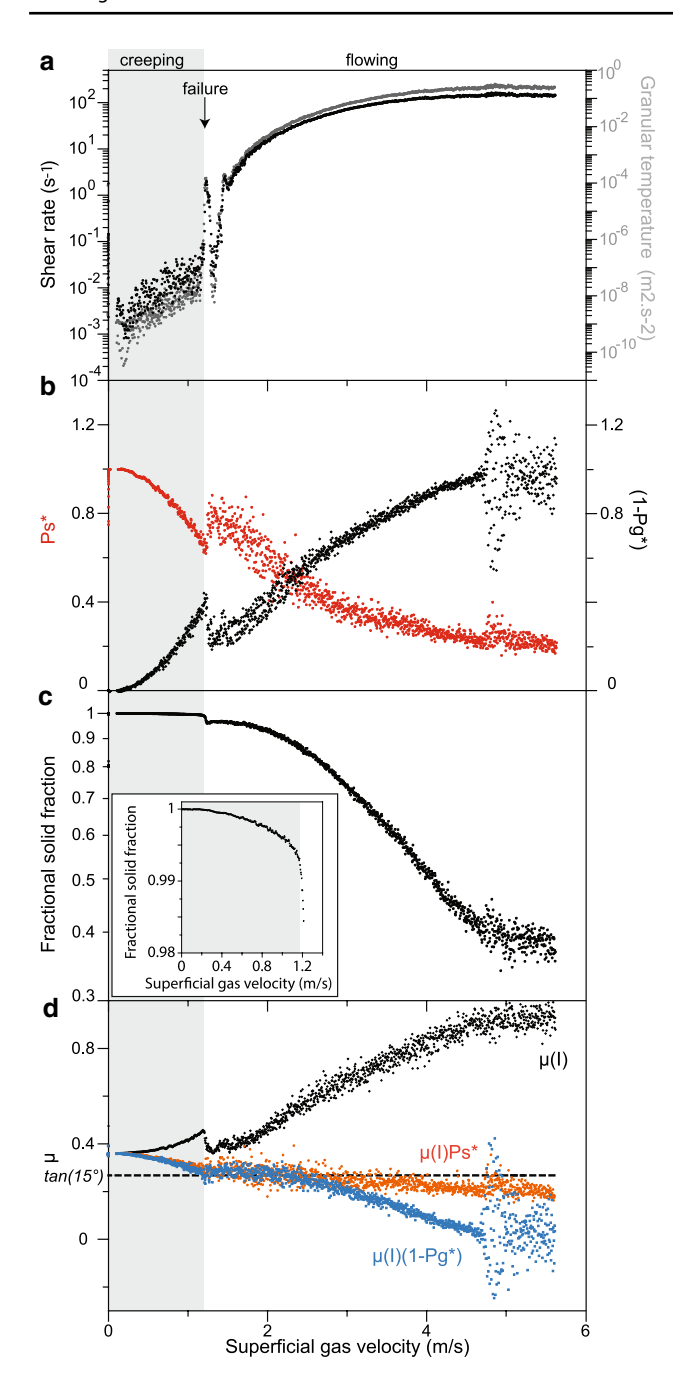
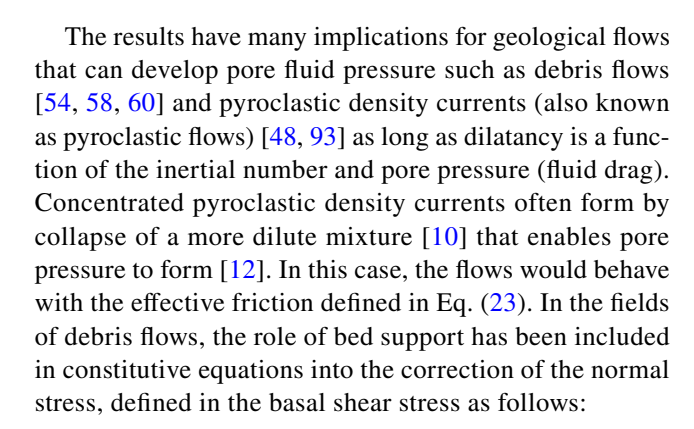


**Fig. 7** Failure of a progressively fluidized bed on a slope. The figure shows the evolution of the shear rate and granular temperature (a), scaled solid pressure  $P_s^*$  and pore pressure  $1-P_g^*$  (b), fractional solid concentration ( $\Phi/\Phi_{\rm start}$ ) (c), friction coefficients  $\mu(I)$ ,  $\mu_{\rm eff}(I,P_s^*)$ ,  $\mu_{\rm eff}(I,P_g^*)$  (d) as a function of superficial velocity

friction coefficient must be equal to the tan(slope). This is verified when calculating the effective friction coefficient using either the  $\mu_{\it eff} \left(I, P_{\it g}^*\right)$  or  $\mu_{\it eff} \left(I, P_{\it s}^*\right)$ , as shown in Fig. 6g.



$$\tau_{base} = \cos(\theta) (\sigma - P_g) \mu_s \tag{24}$$

where  $P_g$  is the pore fluid pressure,  $\sigma$  is the normal stress = solid pressure,  $\mu_s$  is the coulomb friction coefficient of the granular material and  $\theta$  is the slope of the substrate. A similar approach was used by [48] and applied to pyroclastic flows. Without basal slip, the basal friction coefficient is equivalent to the  $\mu(I)$  [40]. Instead, with slip there are differences between the basal and internal friction coefficient [11]. In this work, we do not study the basal friction coefficient and slip. Nevertheless, an equation similar to Eq. (24) can be used to describe the internal shear stress at a given height in the flow. DEM-CFD simulations demonstrate that the friction itself is a non-linear function of the competing effect of the inertial number and most importantly, of the pore pressure. Thus, we write the constitutive equation for the internal shear stress as:

$$\tau = \mu(I)P_s = \mu(I)(\sigma - \alpha P_\sigma) \tag{25}$$

 $\sigma$  is the lithostatic pressure defined as  $\rho gh$ ,  $P_g$  is the pore fluid pressure,  $\alpha$  is the slope correlating the solid to pore fluid pressure (=0.86). Note that a more complex function (non-linear scaling of the solid pressure from pore pressure measurements) could be used, but the relatively good match of the linear fit (R-sq=0.96) is appealing.

While the inertial number increases the friction coefficient, the effect of the pore pressure is thus weakening the effective friction coefficient by the means of reducing the effective normal stress  $\sigma - \alpha P_g$ . The inclusion of the  $\mu(I)$  term is essential because friction in simulated beds increases from 0.35 to 0.9 while the normalized solid pressure is lowered from 1 to 0.2.

This interpretation is analogous to Terzaghi's principle [103], which introduced the concept of effective stress, which is the total stress exerted by the solid "skeleton" minus the pore-fluid pressure in water-saturated soils.

$$\sigma'_{ij} = \sigma_{ij} - P_g \delta_{ij} \tag{26}$$

 $\delta_{ii}$  is the Kronecker's delta.



However, our definition differs from Terzaghi's through the need to use a coefficient  $\alpha$ .

This work is topical to many applications, as illustrated by how pore pressure and the subsequent effective friction can influence failure of a granular flow on an incline. In the next section, we discuss the destabilization of fluidized beds on incline slopes and explore the meaning of the coefficient  $\alpha$ .

## 4.2 Failure of granular flows by progressive fluidization

A bed is placed on a 15° slope (3.5° lower than the angle of repose) and the superficial gas velocity is increased after 2 s following the linear law 0.1 + 0.04\*(time-2). The results and following conclusions are independent of the rate at which the gas velocity was changed (Fig. S2).

Without any superficial velocity the bed experiences creeping, since it rests on a slope lower than the angle of repose. For superficial velocity < 1.2 m/s, the bed remains in the quasistatic regime with a shear rate of  $10^{-4}$ – $10^{-2}$  Hz and a granular temperature that mimics the shear rate data (Fig. 7a). The scaled solid pressure  $P_g^*$  and pore pressure  $1-P_a^*$  data mirror one another (Fig. 7b) while the fractional solid fraction ( $\Phi/\Phi_{start}$ ) declined by 1% (Fig. 7c). Meanwhile, the friction coefficient µ(I) increases from values of 0.36 to 0.46, whereas the effective frictions  $\mu(I,Ps^*)$  and  $\mu(I, Pg^*)$  decline and once reaching ~ tan(15°), the bed fails.

The failure of the bed which follows the increase in pore pressure and subsequent decrease of the effective shear stress is analogous to liquefaction, which operates in saturated soils [59]. Our results are commensurate with the concept of shear strength defined by the Tergazhi-Coulomb criterion, which states that failure can only occur if the effective friction coefficient is < tan(slope). Consequently, dilation of the bed is small enough (up to 1%) for the Tergazhi's principle to be valid.

The failure is followed by a rapid change in all bed properties. The sudden dilation led to a decrease of  $P_a^*$  and subsequent increase of  $P_s^*$ . The bed rapidly recovers and all trends mimic those seen prior to failure. The ability of the bed to fail and accelerate on a slope much smaller than the measured  $\mu(I)$  is captured by the definition of the effective friction coefficient which encapsulate the effective stress. Past the failure point, the bed is flowing and Tergazhi's principle is not the most appropriate description of the effective stress (and effective friction coefficient). Instead, the effective shear stress is better described by Eq. 26 where the proportion of pore pressure alleviating the shear stress is non-unity because shear developed. In other words, even when fully fluidized, the effective shear stress is non-zero because particle interactions generate a normal stress. This is exemplified when plotting the dimensionless solid pressure

Ps\* as a function of the dimensionless pore pressure Pg\* (Fig. 8a).

The introduction of a coefficient in Eq. (25) resembles the description of effective stress introduced by Biot [7], where  $\alpha$ , known as the "Biot effective-stress coefficient" noted  $\alpha_h$ , is the proportion of fluid pressure which will induce the same strains as the total stress. In solid mechanics,  $\alpha_b = 1 - \frac{K_m}{K_s}$ .  $K_m$  is the Bulk modulus of the porous media (or volume compressibility of the matrix) and  $K_s$  is the bulk modulus of the solid (or volume compressibility of the minerals/grains comprising the matrix). Hence, for incompressible mixtures,  $\alpha_b = 1$  and recovers Terzaghi's principle. However, our system is not a dense porous static media with deformable particles. Instead, particles in our simulations are "hard" spheres, where the high spring constant makes the particle overlap in the spring-dashpot model < 1% of their diameter. Therefore, the compressibility of the solid grains is not the cause behind the value of the coefficient  $\alpha$ .

The normal stress (solid pressure) is not vanishing in our simulations because the shear stress is made of both the contact and kinetic contributions (see Eqs. 11, 14, 15), which means that as long as there are velocity fluctuations (even if they were no contacts between particles), the shear stress cannot be null. As shown in Fig. 7a, the granular temperature is  $\sim 0.25 \text{ m}^2/\text{s}^2$  at the end of the simulation, which is very large. For comparison, it is  $\sim 10^{-9}-10^{-10}$  m<sup>2</sup>/ s<sup>2</sup> in the quasistatic regime prior to failure (Fig. 8a). The observation of a non-zero shear stress when the bed is fully fluidized and sheared is commensurate with the predictions of Kinetic Theory [64], which includes the contribution of the granular temperature to the bulk stress tensor. Typically, models that use Terzaghi's principle (usually used for liquid-solid mixtures such as debris flows) make two assumptions: the kinetic stress is null and the solid pressure is isotropic. Both assumptions can be tested in our gas-particle system. First, the contact contribution to the pressure (Ps<sup>c\*</sup>) only is plotted against the dimensionless pore pressure Pg\*, and shows a linear fit with a slope of 0.95 (Fig. 8b). Second, we plot the dimensionless y-component (vertical) of solid pressure from the contact contribution (Psc\*, ) against Pg\*, giving a linear fit with a slope of ~ 1 (Fig. 8c). Thus, we interpret  $\alpha = 0.86$  as the result of both the contribution of the kinetic stress tensor and anisotropy of the solid pressure. This conclusion holds for the range of spring constant (100–10,000 Pa.m), particle-particle restitution (0.1-0.9) and friction coefficients (0.1–0.5) explored (Fig. 8a–c), with specific values of  $\alpha$  span the range of 0.84–0.9 (Fig. 8a). Observing similar deviation from Terzaghi's principle in experimental flows, particularly with high polydispersity, will be highly valuable and yet challenging to obtain as it will require



**34** Page 16 of 25 E. C. P. Breard et al.

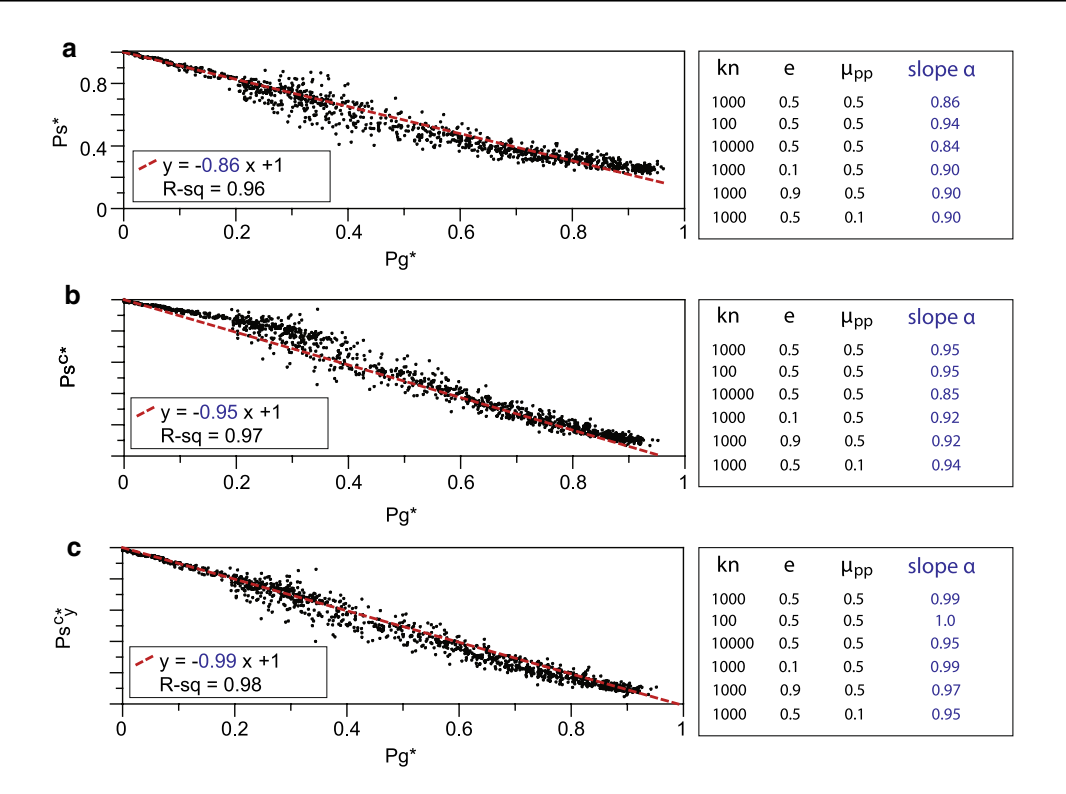


**Fig. 8** Dimensionless solid pressure  $P_s^*$  versus dimensionless gas pore pressure  $P_s^*(\mathbf{a})$ . **b**: Dimensionless solid pressure  $P_s^{c*}$  versus  $P_g^*$ .  $P_s^*$  was calculated from the stress tensor using the collisional contribution only (i.e. excluding the kinetic contribution). In (**a**) and (**b**) the pressure is calculated from the 3D components. In (**c**), the pressure  $P_s^*$  was the y component (normal to the substrate) and includes solely the collisional contribution. A linear fit (red dashed line) and its equa-

tion is illustrated in each figure. The role of the DEM parameters was investigated running 6 variants of the simulation presented in this figure. We varied independently the spring constant "kn" (unit is Pa.m), the particle restitution coefficient "e" and the particle–particle friction coefficient " $\mu_{pp}$ ". The slope  $\alpha$  of the linear fits are shown for each type of plot (a–c)

simultaneous measurements of the (basal) solid pressure in 3D and pore fluid pressure.

# 4.3 Depth-averaged models of granular flows immersed in a fluid.

The role of pore pressure has long been recognized as the essential property controlling the rheology of debris flows modifying the flow rheology from Coulomb solid to a viscous fluid [54, 58–60]. Additionally, the formation of pore pressure during ground shaking can produce liquefaction of soils which facilitates the formation of landslides. Similarly, gas-particle flows can experience a similar effect, where fluidization is a result of pore pressure formation and changes the solid concentration. This process is envisaged in pyroclastic flows, where the presence of high pore pressure has been hypothesized for decades as the origin behind the extreme mobility of these concentrated currents [12–15, 29, 35, 43, 83, 92, 100, 108, 109].

In the past decades, natural granular flows have been simulated using a depth-averaged method that uses the shallow water equations to solve the mass and momentum equations of a single phase (solid) moving across 3D topographies [17, 19, 20, 69, 70, 79, 86], [27]; [47]. The depth-averaged method is particularly useful to understand the behavior or past and future events for quantitative hazard assessment. The strength of a single-phase depth-average model is in their speed and ability to capture the forcing of topography on the flow behavior. However, such approach does not describe the gas-particle coupling (i.e. pore-pressure feedback) and its effect on the effective stresses of the granular mixtures. Recently, an emergent technique relies on two-phase models that capture the interactions between the fluid and solid phases within a saturated mixture, which is particularly relevant to predict the emplacement of debris flows or submarine avalanches [8, 56]. This method is able to capture the inherent compressibility of granular media (i.e. compaction or dilation) using a dilation angle w, which affects the friction and pore-fluid pressure and known as pore-pressure feedback. In these models the shear stress is written as:

$$\tau = \left[\mu(I) + \tan \psi\right] \left[\sigma - P_g\right] \tag{27}$$



$$\nabla \cdot v_s = \dot{\gamma} \tan \psi \tag{28}$$

where the divergence of the solid velocity  $\nabla \cdot v_s$  can estimated as from the temporal changes in solid concentration  $\Phi$ :

$$\nabla \cdot v_s = -\frac{1}{\Phi} \frac{d\Phi}{dt} \tag{29}$$

This implies that in a steady state  $\tan \psi = 0$ . In the simulations we presented in this paper,  $\tan \psi < 0.03 \ \mu(I)$ . Therefore, the contribution of  $\tan \psi$  to the friction coefficient was negligible.

Adapting two-phase flow models for gas-particles flows and including a compressible gas phase could provide a significant leap towards the accurate prediction of the behavior of gas-particle granular flows. Such model would need to capture (a) the dilation and compaction of granular flows and how changes in solid concentration modulates pore-fluid pressure, (b) the non-vanishing of the granular shear stress in highly inertial sheared fluidized beds when the pore pressure equals the "static" solid pressure, and finally (c) role of anisotropy of the flow properties.

Continuum granular flow models like that of Bouchut et al. [8] assumes that granular temperature is negligible in the context of grains immersed in water. We show that in our simulations such assumption would not be valid in our gas-particle simulations, particularly for I > 0.1, for the contribution to the solid pressure was between 1 and 20%.

Therefore, accurate description of gas-particles granular flows in a continuum framework requires a description of velocity fluctuations as a function of other bed properties such as the inertial number, normal and shear stresses, which may be further complexified by the existence of stress and granular temperature anisotropies (e.g. See Fig. 8 in [11].

# 4.4 Suspension and granular rheology of fluidized and non-fluidized beds

In the past, fluidized granular systems were systematically associated with suspensions, which has led to an incorrect prediction of their viscosity [42]. Such assumptions can impede our ability to predict the behavior of fluidized geophysical systems, which encompass mass flows and even magmas. Here, we show the viscosity of a granular bed with and without the presence of pore pressure can be

expressed by accounting for particle collisions. Note that the following section only applies to granular flows with a Stokes number > 1.

When a suspension is sheared, we can express the shear and normal stresses (= solid pressure) as a function of the fluid viscosity, shear rate and solid concentration:

$$\tau = \eta_s(\Phi)\eta_f\dot{\gamma}$$
 and  $P_s = \eta_n(\Phi)\eta_f\dot{\gamma}$  (30)

where  $\eta_s$  and  $\eta_n$  are the dimensionless shear and normal viscosities respectively [101]. As shown in Fig. 5b the sheared non-fluidized and fluidized bed display a dilatancy law that is a function of the inertial number. Thus, we can write dimensionless effective shear and normal viscosities as [1]:

$$\eta_s(\Phi) = \frac{\mu(I(\Phi))}{I(\Phi)^2} \quad \text{and} \quad \eta_n(\Phi) = \frac{1}{I(\Phi)^2}$$
(31)

We can write the friction coefficient of the suspension as a function of the hydrodynamic and contact contributions, combined linearly. The constitutive relation is defined as:

$$\mu(I(\Phi)) = \mu^{c}(\Phi) + \mu^{h}(\Phi) = \mu_{1} + \frac{\mu_{2} - \mu_{1}}{1 + \frac{I_{o}}{I}} + I^{2} + \frac{5}{2} \frac{\Phi_{\text{max}}}{a} I$$
(32)

The terms in red represent the contact contributions which is similar to that of granular media whereas the terms in blue represent the hydrodynamic contribution that recovers the Einstein viscosity at low concentration [32]. This model is in agreement with the unified rheology of viscous suspensions defined by [9].

Here, the dilatancy law observed has an asymptotic form and allows us to write the inertial number as a function of the concentration:

$$\Phi(I) = \frac{\Phi_{\text{max}}}{1 + aI} \text{ or } I = \frac{\Phi_{\text{max}} - \Phi}{a\Phi}$$
 (33)

Hence, the non-dimensional shear viscosity is given by replacing Eqs. (31) and (33) in Eq. (31):

$$\eta_s = \frac{\mu^c}{I^2} + 1 + \frac{5}{2}\Phi \left(1 - \frac{\Phi}{\Phi_m}\right)^{-1} \tag{34a}$$

The same equation can be written as a function of the concentration only using a fitted parameter "a":

$$\eta_s = \mu^c(\Phi)a^2 \left(\frac{\Phi}{\Phi_m - \Phi}\right)^2 + 1 + \frac{5}{2}\Phi\left(1 - \frac{\Phi}{\Phi_m}\right)^{-1}$$
 (34b)

With

$$\mu^{c}(\Phi) = \mu_{1} + \frac{\mu_{2} - \mu_{1}}{1 + \frac{I_{o}}{\left[\frac{\Phi_{m} - \Phi}{a\Phi}\right]}}$$
(35)



**34** Page 18 of 25 E. C. P. Breard et al.

The term  $1+\frac{5}{2}\Phi\left(1-\frac{\Phi}{\Phi_m}\right)^{-1}$  is the hydrodynamic contribution, which recovers that defined by Einstein [1905] at low  $\Phi$  (<0.05):

$$\eta_{s\_Einstein} = 1 + 5\Phi/2 \tag{36}$$

The CG analysis provides measurements of the friction coefficient  $\mu^c$ , inertial number I and solid concentration  $\Phi$ . Thus, we can calculate the shear viscosity using Eq. (34a) (Fig. 9a). The shear viscosity data derived from our simulations is plotted against the Krieger and Dougherty [73] empirical expression of the non-dimensional shear viscosity of non-Newtonian suspensions:

$$\eta_r = \left(1 - \frac{\Phi}{\Phi_m}\right)^{-2.5\Phi_m} \tag{37}$$

Our data collapses onto the empirical curve where  $\Phi_m = 0.583$  for the non-fluidized (Fig. 9a) and fluidized beds

(Fig. 9b). Our results show that the suspension rheology describes efficiently the granular contribution to the viscosity for fluidized and non-fluidized beds.

These results are, to our knowledge, the first quantification of the shear viscosity of fluidized and non-fluidized beds with gravitational forces compared to simulations or experiments where the fluid and particles have the same density [9].

Using the unification of suspension and granular rheology, we simulate fluidized beds prior to bubbling and calculate the mixture viscosity. Multiple experiments with 100 microns particles [44, 72, 90] have shown that gas fluidized bed viscosities could not be explained by classical laws using a pseudo-fluid assumption such as (Eq. 38):

$$\eta_{app}(\Phi) = (1 + 2.8_s \Phi) \eta_f$$
(38)

Gibilaro et al. [42].

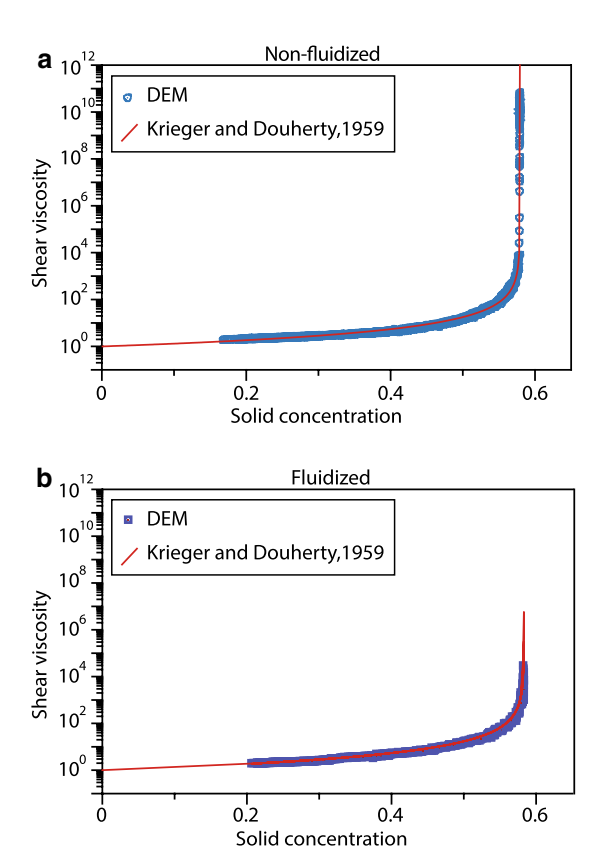
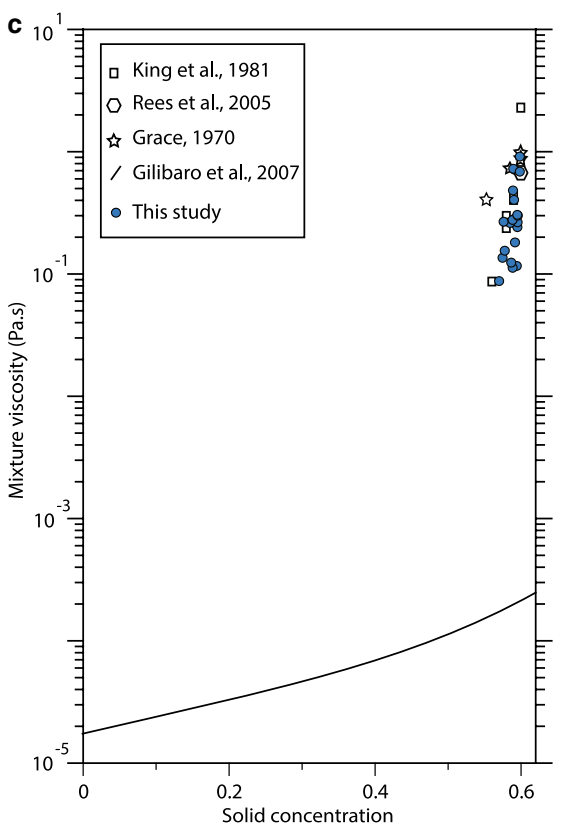


**Fig. 9** Unifying suspension and granular flow rheologies. **a**: Shear viscosity of the non-fluidized bed with the red line representing the empirical formulation of Krieger and Dougherty [73]. Equation (34a) was used to calculate the DEM-CFD data shown in blue. **b**: Shear viscosity of the fluidized bed with the red line representing the empirical formulation of Krieger and Dougherty [73]. We used a maximum concentration value of 0.583 to fit the Krieger and Dougherty law.



Equation (34a) was used to calculate the DEM-CFD data shown in blue. c: Viscosity of the fluidized bed calculated from Eq. (34a) from DEM-CFD simulations of 100 microns beads of density equal to 2500 kg.m<sup>-3</sup> (blue dots), plotted against concentration. Experimental data from [44], King et al. [72] and [90] and a theoretical pseudofluid prediction from Gibilaro et al. [42] are also plotted. Note that the viscosity of air is  $1.8 \times 10^{-5}$  Pa.s at 293 K



The above equation predicted viscosities that were lower than measurements by orders of magnitude. Therefore, Gibilaro et al. [42] attributed the large discrepancy to the particle–particle interactions, lacking in a pseudo fluid assumption. To demonstrate that granular rheology controls viscosity of fluidized beds, we simulated a fluidized bed of 100 microns beads of density equal to that of glass beads (2500 kg.m<sup>-3</sup>) from the onset of minimum fluidization to the onset of bubbling, and estimated the mixture viscosity:

$$\eta_{app} = \eta_s(\Phi)\eta_f \tag{39}$$

The viscosity of the simulated fluidized bed falls within the 0.08–1 Pa.s range (Fig. 9c), which corresponds to the range of measurements from experimental measurements. These results confirm that an accurate description of the shear viscosity that includes the granular rheology can predict the viscosity of fluidized beds.

# 4.5 Application to geophysical flows and implication for substrate erosion

Field evidence indicates re-entrainment of freshly deposited pumice and ash deposits often occurs [30] and can

significantly increase the volume of the current. However, the mechanisms behind the erosion of fine-grained substrate remains an open question [95]. To illustrate how the granular rheology and pore pressure influences the erosion process, we simulated the basal portion of nonfluidized (Fig. 10a) and fluidized beds (Fig. 10b) on a horizontal plane. The simulations illustrate best the high complexity of granular media with and without pore pressure. For instance, the non-fluidized (= pressure-balanced) case displayed effects of non-locality at t=0 s with a friction coefficient in the erodible bed and lower part of the sheared bed case (Fig. 10a) lower than the static coefficient (=0.355). The gradient in shear rate induced small vibrations that propagated from the upper part of the flow onto the bed underneath which is in the quasistatic regime, yielding flowage at  $\mu_{eff} < \mu_s$ . This is known as a non-local granular fluidity effect [68] and was recently attributed to the diffusion of granular temperature [71]. A second after the onset of erosion, the friction coefficient increases  $> \mu_s$ , and few particles from the substrate were incorporated within the basal portion of the flow. Furthermore, in the fluidized case, we simulated the lower portion (lower 0.05 m) of a thick fluidized flow that at t = 0 did not diffuse the pore pressure into the lower bed yet. At that stage, the  $\mu_{eff}$  is about 0.1–0.15 because of the effect of

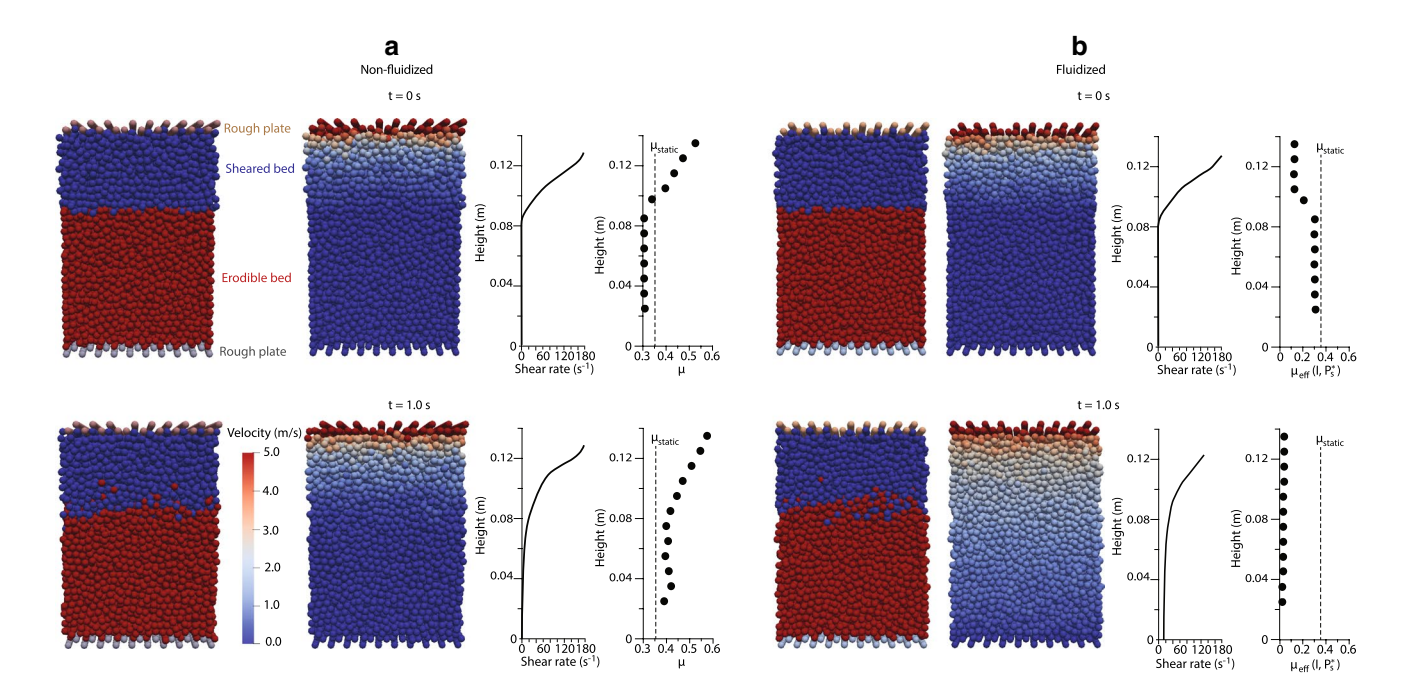
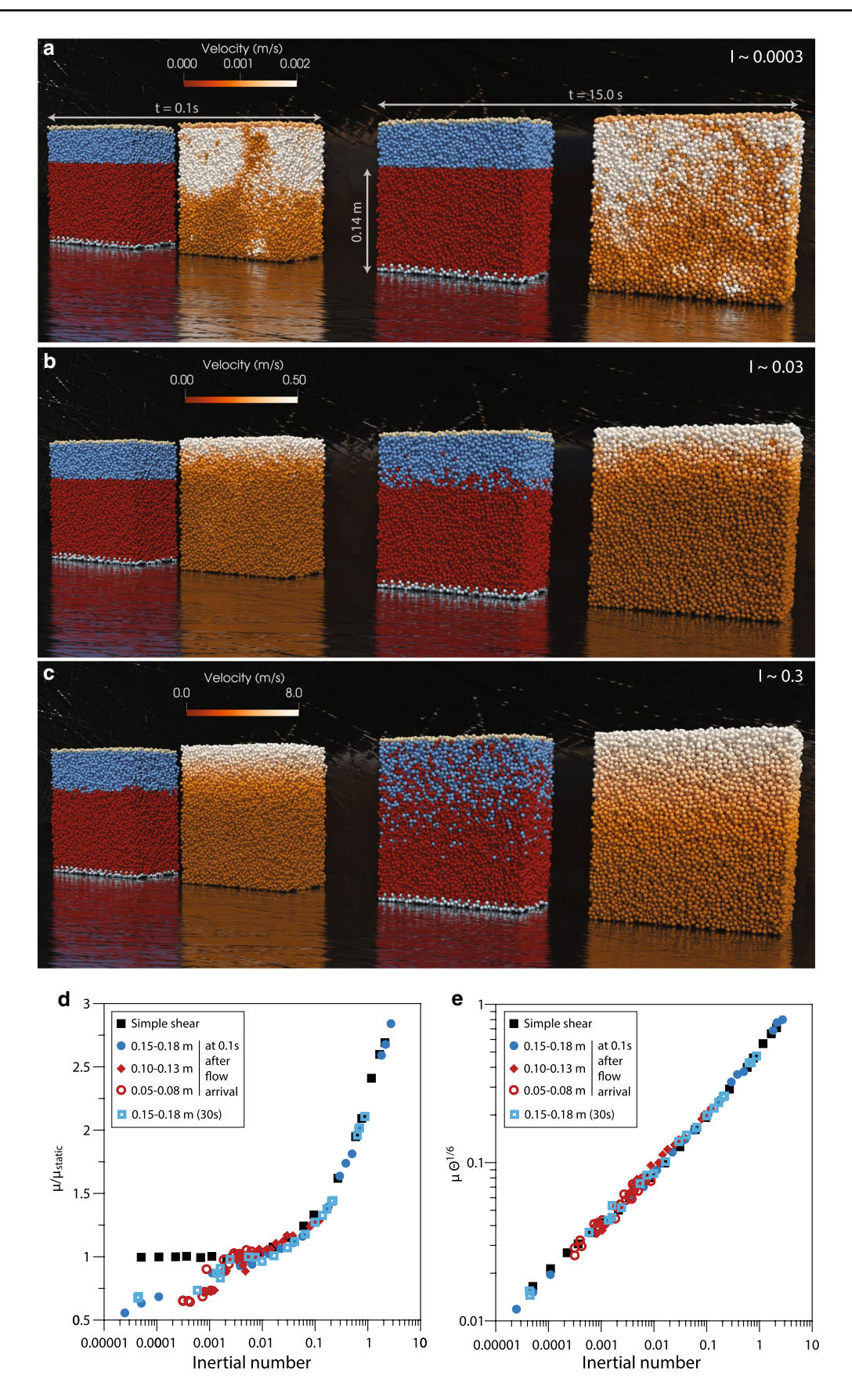


**Fig. 10** Erosion of the substrate by non-fluidized (**a**) and fluidized beds (**b**) with 5 mm particles. **a**: At t=0 s and 1.0 s, the shear rate and friction ( $\mu$ ) coefficient are plotted. **b**: At t=0 s and 1.0 s, the shear rate and effective friction  $\mu_{eff}(I, P_s^*)$  coefficient is plotted. The particle–particle restitution coefficient and contact stiffness was 0.5 and  $10^4$  Pa.m, respectively. The particle–particle restitution coeffi-

cient and contact stiffness was 0.5 and 10<sup>4</sup> Pa.m, respectively. Particles are colored to represent either their group they belong to (rough top plate with light brown, sheared bed with blue, erodible bed in red and bottom rough plate in gray) or their velocity. The color scale used is the same for all plots. The vertical dotted line represents the static friction coefficient of 0.355



Page 20 of 25 E. C. P. Breard et al.





pore pressure, while non-local fluidity affects the erodible bed. Within a second, erosion was well underway with a shear rate two orders of magnitude higher in the former substrate, newly part of the flow. The pore pressure lowered  $\mu_{eff}$  to 0.03–0.06, which enable rapid mobilization of the substrate.

static friction coefficient

We hypothesize that when dense pyroclastic density currents (pyroclastic flows) propagate over a substrate, the flow compacts the substrate because of the rapid increase of the confining solid pressure (Fig. S5). Compaction forces upward diffusion of the excess pore pressure from the substrate into the flow, thus lowering the effective friction coefficient of the substrate. A similar mechanism has been proposed in snow avalanches and debris flows [39, 58, 60]. Through this process, the shear stress applied by the flow upon the substrate can overcome its yield strength (which was weakened first by non-locality) and the substrate will be entrained into the flow. As demonstrated, this erosion process would occur even on shallow slopes, well below the angle of repose of volcanic deposits (~30–40°).

Lowering of the friction coefficient of the substrate is not restricted to granular flows with pore pressure. In fact, the role of non-local effects can be at play in non-fluidized granular flows devoid of excess pore pressure, by simply applying shear gradients upon the substrate, we show that the friction coefficient of the latter is weakened, which in turns promote entrainment even on slopes lower than the static angle of repose.

To demonstrate that velocity fluctuations are the source of the non-local behavior and weakening of the substrate, we defined the dimensionless granular temperature as in Kinetic Theory (Eq. 40):

$$\Theta = \rho_s T_g / P_s \tag{40}$$

Lun et al. [80].

Following the work of Kim and Kamrin [71], we illustrate non-local behavior in a set of 23 simulations where a sheared bed moves atop an erodible substrate with an inertial numbers spanning value of  $10^{-4}$ – $10^{0}$  (Fig. 11a–c). Velocity fluctuations propagate spatially in granular flows through contact forces that can take the form of force chains. Our simulations mimic the arrival of flows spanning quasistatic to inertial regimes and the onset of erosion of the substrate underneath. The development of non-locality is quantified using the scaling of the friction coefficient  $\mu(I,\Theta)$ , which is a function of both the inertial number and the dimensionless granular temperature. The local  $\mu(I)$  – rheology model predicts vanishing shear rate for  $\mu < \mu_{static}$ . However, we observe a creeping region with non-zero shear in such region where the friction coefficient in the substrate deviates from the  $\mu(I)$ (Fig. 11d). The connection between the granular temperature and  $\mu(I)$  becomes clear with the formulation:

$$\mu(I,\Theta) = \left(\frac{\Theta_{loc}(I)}{\Theta}\right)^{1/6} \mu_{loc}(I) \tag{41}$$

where both  $\mu_{loc}(I)$  and  $\Theta_{loc}(I)$  are determined in simple shear flows (i.e. shear cell without non-erodible rough substrate). The collapse of our data and the description presented in Eq. (41) illustrates that as granular temperature increases, the friction coefficient of the granular mixture will be lowered (Fig. 11e).

As demonstrated by Kim and Kamrin [71] (See their Fig. 2), the friction-weakening of a granular media by diffusion of granular temperature is not restricted to region where the inertial number is  $< 10^{-3}$ , but can occur up to  $I \sim 10^{-1}$  (on steep slopes). Such settings are expected to occur in nature, with pyroclastic density currents propagating on steep volcanic slopes and snow-avalanches on snow-clad mountainous flanks.

We have proposed that gas-particle beds with pore pressure (or fluidized beds) rheology combines suspension and granular rheology with the addition of a friction-weakening mechanism ascribable to dilation due to pore pressure diffusion. These results are paramount for understanding the behavior of static and sheared gas-particle granular beds that prevail in many natural environments. Including the contribution of  $\mu(I)$  and excess pore pressure in a description of the effective friction coefficient into numerical models such as depth-averaged models [48, 69] could advance the reliability of the models generally used to assess mass flow hazards by providing robust rheological laws.

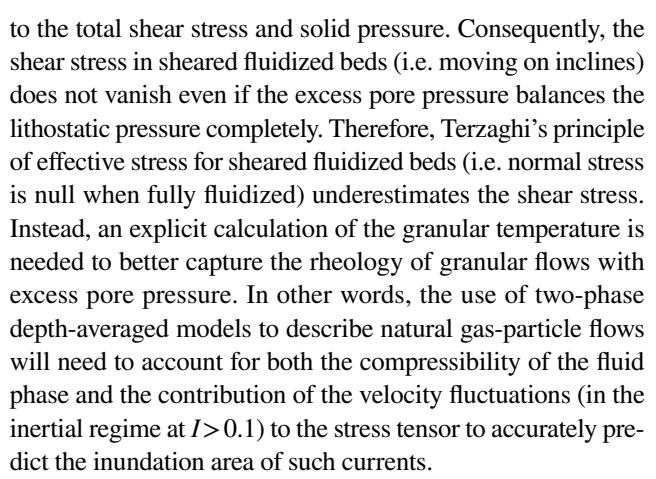


Presently, the rheology of most natural geophysical mixtures, in particular of volcanic ash, remain completely unknown, in comparison with simplified sand or glass bead mixtures [34]. Studies of natural mixtures through experiments will be essential not only to further our understanding of the steady-state rheology, but most importantly, of the transient state as well. In addition, the polydispersity of natural mixtures will influence the flow rheology through size and density segregation, adding to the transience of the mixture rheology. Finally, future analog experiments should focus on measuring granular temperature (even in 2D) to help understand non-locality in granular media and bridge the gap between the discrete and continuum descriptions of granular flows.

#### 5 Conclusion

In this study of gas-fluidized and non-fluidized granular flows we highlighted the main contribution of the pore pressure in the flow rheology. The combination of 3D DEM-CDF and coarse graining (CG) analysis enabled us to study the rheology of sheared granular flows across the whole spectrum of non-fluidized to bubbling fluidized beds. We showed that the  $\mu(I)$ -rheology (friction) and  $\Phi(I)$  (dilatancy) laws across the quasistatic, intermediate and inertial regimes could be recovered by simply running a CG analysis on 2 timesteps (0.1 s apart) in a single simulation and provided similar results compared to time-averaged steady state simulations. The data is described well by the  $\mu(I)$  description of Holyoake and McElwaine [52], which does not predict an asymptotic behavior of the friction at large inertial numbers (>0.2).

Furthermore, in granular flows where pore pressure diffusion occurs (= fluidized bed), an effective friction coefficient governs their behavior and scales with the product of the  $\mu(I)$ and relative pore pressure or solid pressure. Both the  $\mu(I)$  and excess pore pressure have opposing effects on the effective friction coefficient. As the pore pressure increase in a granular flow, drag-induced dilation generates a solid pressure decrease. By being allowed to move more freely, particle collisions induce an increase of the friction coefficient. The addition of drag-induced dilation to granular dynamic dilatancy makes a fluidized bed on a slope behave as if that slope was steeper by a factor scaled with the normal stress reduction. This process is captured by the definition of an effective friction coefficient. Importantly, our results suggest that both the effects of pore pressure and  $\mu(I)$  should be accounted in the constitutive equations of gas-particle flows where pore pressure can form, as it is commonly done in the debris-flow community. In addition, on an incline, fluidized beds dilate because of particle collision. As a result, the kinetic stress tensor (which is a function of granular temperature) has a large contribution (up to 20%)



Simulations illuminate how the viscosity of non-fluidized and fluidized beds could be expressed as a function of the contact and hydrodynamic contributions, thus unifying the suspension and granular rheology. Using a similar description, we showed that the viscosity of fluidized beds could be predicted and match experiments.

Finally, we illustrated the role of pore pressure beyond its modification of the sheared bed rheology, and in particular, its effectiveness for entrainment of an erodible substrate. We show that non-local effects occur when a granular flow propagates over an erodible substrate and that such behavior is the result of the diffusion of velocity fluctuations. Beyond the fundamental applications of this work, these results further our understanding of natural granular systems. They are particularly topical for geophysical flows where excess pore pressure can drastically affect flow mechanics (i.e. pyroclastic density currents and snow avalanches).

**Supplementary Information** The online version contains supplementary material available at https://doi.org/10.1007/s10035-021-01192-5.

Acknowledgements Financial support was provided by the National Science Foundation (EAR 1852569 and EAR 1650382) and MCIU/AEI/FEDER, UE (Grant No. PGC2018 336 097842-B-100). The research of LF was supported by the Royal Society of New Zealand (MAU1712). The research of MT was supported by La Caixa. The data supporting the conclusions are shown in the figures and tables presented. Interested readers will find additional data in the supporting information. On request the authors can also provide more specific results obtained from the experimental and numerical studies used to produce the figures.

ECPB thanks F. Bouchut and M. Yang for useful discussions.

#### **Declarations**

Conflict of interest The authors declare that they have no conflict of interest.

**Code availability** The code used to produce the CFD is publicly available at https://mfix.netl.doe.gov.



- 1. Andreotti, B., Forterre, Y., Pouliquen, O.: Granular media: between fluid and solid. Cambridge, New York (2013)
- Aranson, I.S., Tsimring, L.S.: Continuum theory of partially fluidized granular flows. Phys. Rev. E 65(6), 061303 (2002)
- Babic, M.: Average balance equations for granular materials. Int. J. Eng. Sci. 35(5), 523–548 (1997)
- 4. Barker, T., Schaeffer, D.G., Shearer, M., Gray, J.M.N.T.: Well-posed continuum equations for granular flow with compressibility and  $\mu(I)$ -rheology. Proc. R. Soc. A, (2017). https://doi.org/10.1098/rspa.2016.0846
- Bergantz, G.W., Schleicher, J.M., Burgisser, A.: On the kinematics and dynamics of crystal-rich systems. J. Geophys. Res. Solid Earth 122(8), 6131–6159 (2017)
- Beverloo, W.A., Leniger, H.A., van de Velde, J.: The flow of granular solids through orifices. Chem. Eng. Sc. 15(3-4), 260-269 (1961)
- Biot, M.A.: Mechanics of deformation and acoustic propagation in porous media. J. Appl. Phys. 33(4), 1482–1498 (1962)
- Bouchut, F., Fernández-Nieto, E.D., Mangeney, A., Narbona-Reina, G.: A two-phase two-layer model for fluidized granular flows with dilatancy effects. J. Fluid. Mech. 801, 166–221 (2016)
- Boyer, F., Guazzelli, É., Pouliquen, O.: Unifying suspension and granular rheology. Phys. Rev. Lett. 107(18), 188301 (2011)
- Branney, M., Kokelaar, P.: Pyroclastic density currents and the sedimentation of ignimbrites, p. 143. Geological Society Publishing House, Bath, United Kingdom (2002)
- Breard, E.C.P., Dufek, J., Fullard, L., Carrara, A. (2020). The basal friction coefficient of granular flows with and without excess pore pressure: implications for pyroclastic density currents, water-rich debris flows, and rock and submarine avalanches. J. Geophys. Res. Solid Earth 125(12), e2020JB020203
- Breard, E.C.P., Dufek, J., Lube, G.: Enhanced mobility in concentrated pyroclastic density currents: an examination of a self-fluidization mechanism. Geophys. R. Lett. 45, 654–664 (2017)
- Breard, E.C.P., Dufek, J., Roche, O.: Continuum modeling of pressure-balanced and fluidized granular flows in 2-D: comparison with glass bead experiments and implications for concentrated pyroclastic density currents. J. Geophys. Res. Solid Earth 124(6), 5557–5583 (2019)
- Breard, E.C.P., Jones, J.R., Fullard, L., Lube, G., Davies, C., Dufek, J.: The permeability of volcanic mixtures—implications for pyroclastic currents. J. Geophys. Res. Solid Earth 124(2), 1343–1360 (2019)
- Brown, M.C.: Nuees ardentes and fluidization. Am. J. Sci. 260(6), 467–470 (1962)
- Calder, E.S., Sparks, R.S.J., Gardeweg, M.C.: Erosion, transport and segregation of pumice and lithic clasts in pyroclastic flows inferred from ignimbrite at Lascar Volcano, Chile. J. Volcanol. Geotherm. Res. 104(1-4), 201-235 (2000)
- Capra, L., Manea, V.C., Manea, M., Norini, G.: The importance of digital elevation model resolution on granular flow simulations; a test case for Colima Volcano using TITAN2D computational routine. Nat. Hazards 59(2), 665–680 (2011)
- Carrara, A., Burgisser, A., Bergantz, G.W.: Lubrication effects on magmatic mush dynamics. J. Volcanol. Geotherm. Res. 380, 19–30 (2019)
- Charbonnier, S.J., Germa, A., Connor, C.B., Gertisser, R., Preece, K., Komorowski, J.-C., Lavigne, F., Dixon, T., Connor, L.: Evaluation of the impact of the 2010 pyroclastic density currents at Merapi Volcano from high-resolution satellite

- imagery, field investigations and numerical simulations. J. Volcanol. Geotherm. Res. **261**, 295–315 (2013)
- Charbonnier, S.J., Gertisser, R.: Numerical simulations of block-and-ash flows using the Titan2D flow model; examples from the 2006 eruption of Merapi Volcano, Java, Indonesia. Bull. Volcanol. 71(8), 953–959 (2009)
- 21. Chen, J.C., Grace, J.R., Golriz, M.R.: Heat transfer in fluidized beds: design methods. Powder Technol. **150**(2), 123–132 (2005)
- Chialvo, S., Sun, J., Sundaresan, S.: Bridging the rheology of granular flows in three regimes. Phys. Rev. E 85(2), 021305 (2012)
- Chialvo, S., Sundaresan, S.: A modified kinetic theory for frictional granular flows in dense and dilute regimes. Phys. Fluid 25(7), 070603 (2013)
- 24. Cleary, P.W., Sawley, M.L.: DEM modelling of industrial granular flows: 3D case studies and the effect of particle shape on hopper discharge. Appl. Math. Model. **26**(2), 89–111 (2002)
- 25. Coulomb, C.A.: Theorie des machines simples. Acad. Sci. 166(10) (1781)
- da Cruz, F., Emam, S., Prochnow, M., Roux, J.-N., Chevoir, F.: Rheophysics of dense granular materials: discrete simulation of plane shear flows. Phys. Rev. E (72):021309 (2005)
- de' Michieli Vitturi, M., Esposti Ongaro, T., Lari, G., Aravena,
   A.: IMEX\_SfloW2D 1.0: a depth-averaged numerical flow model for pyroclastic avalanches Geosci. Model Dev. 12(1), 581 595 (2019)
- Druitt, T.H., Avard, G., Bruni, G., Lettieri, P., Maez, F.: Gas retention in fine-grained pyroclastic flow materials at high temperatures. Bull. Volcanol. 69(8), 881–901 (2007)
- Druitt, T.H., Bruni, G., Lettieri, P., Yates, J.G.: The fluidization behaviour of ignimbrite at high temperature and with mechanical agitation. Geophys. R. Lett. 31(2) (2004)
- Druitt, T.H., Calder, E.S., Cole, P.D., Hoblitt, R.P., Loughlin, S.C., Norton, G.E., Ritchie, L.J., Sparks, R.S.J., Voight, B.: Small-volume, highly mobile pyroclastic flows formed by rapid sedimentation from pyroclastic surges at Soufriere Hills Volcano, Montserrat; an important volcanic hazard. Mem. Geol. Soc. Lond. 21, 263–279 (2002)
- Edwards, A.N., Gray, J.M.N.T.: Erosion-deposition waves in shallow granular free-surface flows. J. Fluid. Mech. 762, 35–67 (2014)
- Einstein, A.: Über die von der molekularkinetischen Theorie der Wärme geforderte Bewegung von in ruhenden Flüssigkeiten suspendierten Teilchen. Ann. Phys. 322(8), 549–560 (1905)
- Fall, A., Ovarlez, G., Hautemayou, D., Mézière, C., Roux, J.N., Chevoir, F.: Dry granular flows: rheological measurements of the μ(I)-rheology. J. Rheol. 59(4), 1065–1080 (2015)
- Forterre, Y., Pouliquen, O.: Flows of dense granular media.
   Annu. Rev. Fluid Mech. 40(1), 1–24 (2008)
- Freundt, A.: The formation of high-grade ignimbrites, I: experiments on high- and low-concentration transport systems containing sticky particles. Bull. Volcanol. 59(6), 414–435 (1998)
- Fullard, L., Breard, E., Davies, C., Lagrée, P.-Y., Popinet, S., Lube, G.: Testing the μ(I) granular rheology against experimental silo data. EPJ Web Conf. 140, 11002 (2017)
- Gallier, S., Lemaire, E., Peters, F., Lobry, L.: Rheology of sheared suspensions of rough frictional particles. J. Fluid. Mech. 757, 514–549 (2014)
- 38. Garg, R., Galvin, J., Li, T., Pannala, S.: Open-source MFIX-DEM software for gas-solids flows: part I—verification studies. Powder Technol. **220**, 122–137 (2012)
- Gauer, P., Issler, D.: Possible erosion mechanisms in snow avalanches. Ann. Glaciol. 38, 384–392 (2017)
- 40. MiDi, G.D.R.: Eur. Phys. J. E 14, 341 (2004)
- 41. Geldart, D.: Types of gas fluidization. Powder Technol. **7**(5), 285–292 (1973)



**34** Page 24 of 25 E. C. P. Breard et al.

 Gibilaro, L.G., Gallucci, K., Di Felice, R., Pagliai, P.: On the apparent viscosity of a fluidized bed. Chem. Eng. Sc. 62(1-2), 294-300 (2007)

- 43. Girolami, L., Druitt, T.H., Roche, O.: Dynamics of laboratory ash flows. International Union of Geodesy and Geophysics General Assembly = Union Geodesique et Geophysique Internationale Comptes Rendus de la ...Assemblee Generale 24 (2007)
- Grace, J.R.: The viscosity of fluidized beds. Can. J. Chem. Eng. 48(1), 30–33 (1970)
- Grace, J.R.: Agricola aground: characterization and interpretation of fluidization phenomena. AIChE Symp. Ser. 289(88), 1–16 (1992)
- Gu, Y., Ozel, A., Sundaresan, S.: Rheology of granular materials with size distributions across dense-flow regimes. Powder Technol. 295(Supplement C), 322–329 (2016)
- Gueugneau, V., Kelfoun, K., Charbonnier, S., Germa, A., Carazzo, G.: Dynamics and impacts of the May 8th, 1902 pyroclastic current at Mount Pelée (Martinique): new insights from numerical modeling. Front. Earth Sci. 8(279) (2020)
- Gueugneau, V., Kelfoun, K., Roche, O., Chupin, L.: Effects of pore pressure in pyroclastic flows: numerical simulation and experimental validation. Geophys. R. Lett. 44(5), 2194–2202 (2017)
- 49. Guo, N., Zhao, J.: The signature of shear-induced anisotropy in granular media. Comput. Geotech. 47, 1–15 (2013)
- Hartkamp, R., Ghosh, A., Weinhart, T., Luding, S.: A study of the anisotropy of stress in a fluid confined in a nanochannel. J. Chem. Phys. 137(4), 044711 (2012)
- Henann, D.L., Kamrin, K.: A predictive, size-dependent continuum model for dense granular flows. Proc. Natl Acad. Sci. 110(17), 6730 (2013)
- 52. Holyoake, A.J., McElwaine, J.N.: High-speed granular chute flows. J. Fluid. Mech. **710**, 35–71 (2012)
- Hutter, K.: Geophysical granular and particle-laden flows: review of the field Philos. Trans. R. Soc. A Math. Phys. Eng. Sci. 363, 1832–1497 (2005)
- Iverson, R.H.: The physics of debris flows. Rev. Geophys. 35(3), 245–296 (1997)
- Iverson, R.M.: Regulation of landslide motion by dilatancy and pore pressure feedback. J. Geophys. Res. Earth Surf. 110(F2) (2005)
- Iverson, R.M., George, D.L.: A depth-averaged debris-flow model that includes the effects of evolving dilatancy. I. Physical basis. Proc. R. Soc. A Math. Phys. Eng. Sc. 470(2170), 20130819 (2014)
- Iverson, R.M., Lahusen, R.G.: Dynamic pore-pressure fluctuations in rapidly shearing granular materials. Science 246(4831) (1989)
- Iverson, R.M., Logan, M., LaHusen, R.G., Berti, M.: The perfect debris flow? Aggregated results from 28 large-scale experiments. J. Geophys. Res. Earth Surf. 115(F3) (2010)
- Iverson, R.M., Reid, M.E., LaHusen, R.G.: Debris-flow mobilization from landslides. Annu. Rev. Earth Planet. Sci. 25(1), 85–138 (1997)
- Iverson, R.M., Reid, M.E., Logan, M., LaHusen, R.G., Godt, J.W., Griswold, J.P.: Positive feedback and momentum growth during debris-flow entrainment of wet bed sediment. Nat. Geosci. 4, 116 (2010)
- Iverson, R.M., Vallance, J.W.: New views of granular mass flows. Geology 29(2), 115–118 (2001)
- Jaeger, H.M., Nagel, S.R.: Physics of the granular state. Science 255(5051), 1523 (1992)
- Janda, A., Zuriguel, I., Garcimartín, A., Maza, D.: Clogging of granular materials in narrow vertical pipes discharged at constant velocity. Granular Matter 17(5), 545–551 (2015)

- Jessop, D.E., Hogg, A.J., Gilbertson, M.A., Schoof, C.: Steady and unsteady fluidised granular flows down slopes. J. Fluid. Mech. 827, 67–120 (2017)
- Jop, P., Forterre, Y., Pouliquen, O.: Crucial role of sidewalls in granular surface flows: consequences for the rheology. J. Fluid. Mech. 541, 167–192 (2005)
- 66. Jop, P., Forterre, Y., Pouliquen, O.: A constitutive law for dense granular flows. Nature **441**, 727–730 (2006)
- 67. Kamrin, K., Henann, D.L.: Nonlocal modeling of granular flows down inclines. Soft Matter 11, 179–185 (2015)
- Kamrin, K., Koval, G.: Nonlocal constitutive relation for steady granular flow. Phys. Rev. Lett. 108(17), 178301 (2012)
- Kelfoun, K.: Suitability of simple rheological laws for the numerical simulation of dense pyroclastic flows and long-runout volcanic avalanches. J. Geophys. Res. 116(B8) (2011)
- Kelfoun, K.: A two-layer depth-averaged model for both the dilute and the concentrated parts of pyroclastic currents. J. Geophys. Res. Solid Earth 122(6), 4293–4311 (2017)
- Kim, S., Kamrin, K.: Power-law scaling in granular rheology across flow geometries. Phys. Rev. Lett. 125(8), 088002 (2020)
- King, D.F., Mitchell, F.R.G., Harrison, D.: Dense phase viscosities of fluidised beds at elevated pressures. Powder Technol. 28(1), 55–58 (1981)
- Krieger, I.M., Dougherty, T.J.: A mechanism for Non-Newtonian flow in suspensions of rigid spheres. Trans. Soc. Rheol. 3(1), 137–152 (1959)
- 74. Kunii, D., Levespiel, O.: Fluidization engineering, 2nd edn. Butterworth-Heinemann (1991)
- Langston, P.A., Tüzün, U., Heyes, D.M.: Discrete element simulation of granular flow in 2D and 3D hoppers: dependence of discharge rate and wall stress on particle interactions. Chem. Eng. Sci. 50(6), 967–987 (1995)
- Li, T., Garg, R., Galvin, J., Pannala, S.: Open-source MFIX-DEM software for gas-solids flows: part II—validation studies. Powder Technol 220(Supplement C), 138–150 (2012)
- Lube, G., Breard, E.C.P., Esposti-Ongaro, T., Dufek, J., Brand,
   B.: Multiphase flow behaviour and hazard prediction of pyroclastic density currents. Nat. Rev. Earth Environ. 1(7), 348–365 (2020)
- Lube, G., Breard, E.C.P., Jones, J., Fullard, L., Dufek, J., Cronin, S.J., Wang, T.: Generation of air lubrication within pyroclastic density currents. Nat. Geosci. 12(5), 381–386 (2019)
- Lucas, A., Mangeney, A., Ampuero, J.P.: Frictional velocityweakening in landslides on Earth and on other planetary bodies. Nat. Commun. 5(1), 3417 (2014)
- Lun, C.K.K., Savage, S.B., Jeffrey, D.J., Chepurniy, N.: Kinetic theories for granular flow: inelastic particles in Couette flow and slightly inelastic particles in a general flowfield. J. Fluid. Mech. 140, 223–256 (1984)
- 81. Marzougui, D., Chareyre, B., Chauchat, J.: Microscopic origins of shear stress in dense fluid–grain mixtures. Granular Matter **17**(3), 297–309 (2015)
- 82. Mickley, H.S., Fairbanks, D.F.: Mechanism of heat transfer to fluidized beds. AIChE J. 1(3), 374–384 (1955)
- Montserrat, S., Tamburrino, A., Roche, O., Niño, Y.: Pore fluid pressure diffusion in defluidizing granular columns. J. Geophys. Res. Earth Surf. 117(F2) (2012)
- Musser, J., Vaidheeswaran, A., Clarke, M.A.: MFIX Documentation volume 3: verification and validation manual; 3rd (ed.).
   NETL-PUB-22050; NETL Technical Report Series; U.S. Department of Energy, National Energy Technology Laboratory: Morgantown, WV (2021)
- Ness, C., Sun, J.: Flow regime transitions in dense non-Brownian suspensions: Rheology, microstructural characterization, and constitutive modeling. Phys. Rev. E 91(1), 012201 (2015)



- 86. Ogburn, S.E., Calder, E.S.: The relative effectiveness of empirical and physical models for simulating the dense undercurrent of pyroclastic flows under different emplacement conditions. Front.
- 87. Pailha, M., Nicolas, M., Pouliquen, O.: Initiation of underwater granular avalanches: Influence of the initial volume fraction. Phys. Fluid **20**(11), 111701 (2008)

Earth Sci. 5(83) (2017)

- 88. Pouliquen, O., Vallance, J.W.: Segregation induced instabilities of granular fronts. Chaos **3**(9), 621–630 (1999)
- Queteschiner, D., Lichtenegger, T., Schneiderbauer, S., Pirker,
   S.: Adaptive coarse-graining for large-scale DEM simulations.
   In: 12th International Conference on CFD in Oil & Gas, Metallurgical and Process Industries. Norway (2017)
- Rees, A.C., Davidson, J.F., Dennis, J.S., Hayhurst, A.N.: The rise of a buoyant sphere in a gas-fluidized bed. Chem. Eng. Sci. 60(4), 1143–1153 (2005)
- Reynolds, O.: On the dilatancy of media composed of rigid particles in contact. Philos. Mag. Ser. 5(20), 469 (1885)
- Roche, O.: Depositional processes and gas pore pressure in pyroclastic flows: an experimental perspective. Bull. Volcanol. 74(8), 1807–1820 (2012)
- Roche, O., Buesch, D.C., Valentine, G.A.: Slow-moving and fartravelled dense pyroclastic flows during the Peach Spring supereruption. Nat. Commun. 7 (2016)
- Roche, O., Gilbertson, M.A., Phillips, J.C., Sparks, R.S.J.: Inviscid behaviour of fines-rich pyroclastic flows inferred from experiments on gas-particle mixtures. Earth Planet. Sci. Lett. 240(2), 401–414 (2005)
- Roche, O., Nino, Y., Mangeney, A., Brand, B., Pollock, N., Valentine, G.A.: Dynamic pore-pressure variations induce substrate erosion by pyroclastic flows. Geology 41(10), 1107–1110 (2013)
- 96. Roux, R., Radjai, F.: Physics of dry granular media. Springer, pp. 229–236 (1998)
- Rubio-Largo, S.M., Janda, A., Maza, D., Zuriguel, I., Hidalgo, R.C.: Disentangling the free-fall arch paradox in silo discharge. Phys. Rev. Lett. (2015)
- 98. Schoefield, A., Wroth, P.: Critical state soil mechanics. McGraw-Hill (1968)
- Smith, G.M., Williams, R., Rowley, P.J., Parsons, D.R.: Investigation of variable aeration of monodisperse mixtures: implications for pyroclastic density currents. Bull. Volcanol. 80(8), 67 (2018)
- Sparks, R.S.J.: Grain size variations in ignimbrites and implications for the transport of pyroclastic flows. Sedimentology 23(2), 147–188 (1976)

- Stickel, J.J., Powell, R.L.: FLUID MECHANICS AND RHE-OLOGY OF DENSE SUSPENSIONS. Annu. Rev. Fluid Mech. 37(1), 129–149 (2005)
- 102. Sutherland, W.: The viscosity of gases and molecular force. Philos. Mag. **36**, 507–531 (1893)
- Terzaghi, K.: The shearing resistance of saturated soils and the angle between the planes of shear. In: Proceedings of the first international conference on soil mechanics and foundation engineering, D-7 (1936)
- Thornton, A., Weinhart, T., Luding, S., Bokhove, O.: Modeling of the particle size segregation: calibration using the discrete particle method. Int. J. Mod. Phys. C 23(08), 1240014 (2012)
- Weinhart, T., Hartkamp, R., Thornton, A.R., Luding, S.: Coarse-grained local and objective continuum description of three-dimensional granular flows down an inclined surface. Phys. Fluid 25(7), 070605 (2013)
- Weinhart, T., Labra, C., Luding, S., Ooi, J.Y.: Influence of coarse-graining parameters on the analysis of DEM simulations of silo flow. Powder Technol. 293, 138–148 (2016)
- Weinhart, T., Thornton, A.R., Luding, S., Bokhove, O.: Closure relations for shallow granular flows from particle simulations. Granular Matter 14(4), 531–552 (2012)
- Wilson, C.J.N.: The role of fluidization in the emplacement of pyroclastic flows: an experimental approach. J. Volcanol. Geotherm. Res. 8, 231–249 (1980)
- Wilson, C.J.N.: The role of fluidization in the emplacement of pyroclastic flows, 2: experimental results and their interpretation. J. Volcanol. Geotherm. Res. 20(1), 55–84 (1984)
- Wood, D.M.: Soil behaviour and critical state soil mechanics.
   Cambridge University Press (1990)
- Wood, D.M.: Introduction: models and soil mechanics. In: Wood,
   D.M. (ed.) Soil behaviour and critical state soil mechanics, pp.
   1–36. Cambridge University Press, Cambridge (1991)
- 112. Yang, M., Taiebat, M., Mutabaruka, P., Radjaï, F.: Evolution of granular materials under isochoric cyclic simple shearing. Phys. Rev. E 103(3), 032904 (2021)
- Zhang, Q., Kamrin, K.: Microscopic description of the granular fluidity field in nonlocal flow modeling. Phys. Rev. Lett. 118(5), 058001 (2017)

**Publisher's Note** Springer Nature remains neutral with regard to jurisdictional claims in published maps and institutional affiliations.

